AGU PUBLICATIONS

Journal of Advances in Modeling Earth Systems

RESEARCH ARTICLE
10.1002/2015MS000603

Second-order finite volume with hydrostatic reconstruction for tsunami simulation

S. Clain[1], C. Reis[1,2], R. Costa[1], J. Figueiredo[1], M. A. Baptista[2,3], and J. M. Miranda[2,4]

[1]Centro de Matemática, Universidade do Minho, Braga, Portugal, [2]Instituto Dom Luiz, Faculdade de Ciências, Universidade de Lisboa, Lisboa, Portugal, [3]Instituto Português do Mar e da Atmosfera, Lisboa, Portugal, [4]Instituto Superior de Engenharia de Lisboa, Lisboa, Portugal

Key Points:
- Second-order finite volume scheme with hydrostatic reconstruction
- Nonconservative flux
- Application to tsunami

Correspondence to:
S. Clain,
clain@math.uminho.pt

Citation:
Clain, S., C. Reis, R. Costa, J. Figueiredo, M. A. Baptista, and J. M. Miranda (2016), Second-order finite volume with hydrostatic reconstruction for tsunami simulation, *J. Adv. Model. Earth Syst.*, *8*, 1691–1713, doi:10.1002/2015MS000603.

Received 8 DEC 2015
Accepted 1 OCT 2016
Accepted article online 6 OCT 2016
Published online 27 OCT 2016

Abstract Tsunami modeling commonly accepts the shallow water system as governing equations where the major difficulty is the correct treatment of the nonconservative term due to bathymetry variations. The finite volume method for solving the shallow water equations with such source terms has received great attention in the two last decades. The built-in conservation property, the capacity to correctly treat discontinuities, and the ability to handle complex bathymetry configurations preserving some steady state configurations (well-balanced scheme) make the method very efficient. Nevertheless, it is still a challenge to build an efficient numerical scheme, with very few numerical artifacts (e.g., small numerical diffusion, correct propagation of the discontinuities, accuracy, and robustness), to be used in an operational environment, and that is able to better capture the dynamics of the wet-dry interface and the physical phenomena that occur in the inundation area. In the first part of this paper, we present a new second-order finite volume code. The code is developed for the shallow water equations with a nonconservative term based on the hydrostatic reconstruction technology to achieve a well-balanced scheme and an adequate dry/wet interface treatment. A detailed presentation of the numerical method is given. In the second part of the paper, we highlight the advantages of the new numerical technique. We benchmark the numerical code against analytical, experimental, and field results to assess the robustness and the accuracy of the numerical code. Finally, we use the 28 February 1969 North East Atlantic tsunami to check the performance of the code with real data.

1. Introduction

Tsunamis simulations are within the shallow water equations (SWE) conditions of applicability. Three types of numerical schemes are used to solve the SWE: the finite difference scheme, the finite volume scheme, and the finite element scheme.

These solvers tackle the shallow water equations, in Cartesian or spherical coordinates, with additional source terms to account for the bathymetry variation, the friction, or the turbulence.

The finite difference scheme was the first to simulate tsunami propagation due to its simplicity in the structured grids context (MOST) [*Titov and González*, 1997], TUNAMI [*Goto et al.*, 1997; *Imamura et al.*, 2006], or COMCOT [*Liu et al.*, 1998]. Nevertheless, the finite difference schemes suffer three drawbacks: (1) they are not entirely conservative (the total mass is not preserved, even if the losses can be under 5%); (2) they are not well-balanced (the configuration of ocean at rest is not maintained); and, at last, (3) the use of a formulation based on the primitive variables (height and velocity) to reduce the numerical effects of the bathymetry source term that provide erroneous results when discontinuities are involved. The nonconservative system using the velocity as an unknown function would have difficulties modeling breaking waves since only the conservative formulation provides the correct Rankine-Hugoniot conditions. To quote *George* [2004]: *Hou and LeFloch* [1994] proved that if a nonconservative method is used, it converges to the wrong solution if it contains a shock wave. Use of a naive method can lead to spurious oscillations near a shock wave, computing shocks with the wrong strength, or propagating shocks with the wrong speed [see also *LeVeque*, 2002; *Toro*, 2001].

Moreover, second-order versions create some spurious oscillations in the vicinity of discontinuities and a large amount of artificial viscosity is added to stabilize the scheme leading to a dramatic reduction of the accuracy [*Zhou et al.*, 2002; *Gallouët et al.*, 2003; *Nikolos and Delis*, 2009].

Since the nineties, the finite volume method has become a more efficient technique to solve hyperbolic nonlinear systems for complex modeling in atmospheric sciences and geophysical fluid dynamics [*Zhou et al*., 2015] or hydrological models [*Salah et al*., 2010]. Numerical codes for tsunami simulation using the finite volume scheme were developed and implemented such as ANUGA [*Roberts et al*., 2010] and GEOCLAW [*Berger et al*., 2011, and *LeVeque et al*., 2011], among others. They preserve mass and the use of conservative variables guarantees the validity of the shock propagation. GEOCLAW is based on the f-wave decomposition which integrates the bathymetry jump at the cell's interface [*George and LeVeque*, 2006] while ANUGA uses the Divergence Form for Bed slope source term (tagged DFB) developed in *Valiani and Begnudelli* [2006] to take the hydrological jumps into account.

In this study, we introduce and implement a different finite volume technology which enables to deal with varying bathymetry and provides high-accuracy solutions. The hydrostatic reconstruction method [*Audusse et al*., 2004; *Berthon and Fouchet*, 2012] became a very popular and simple numerical technique for handling both the topography and the dry/wet interface. One critical aspect of tsunami simulations is the variation of the bathymetry where the nonconservative term has to be discretized with caution. Indeed, some steady state solutions have to be preserved at the discrete level leading to the so-called *C*-property [*Bermúdez and Vázquez*, 1994; *Bermúdez et al*., 1998] and the well-balanced concept [*Greenberg and Leroux*, 1996; *Duran et al*., 2013]. If not preserved, the scheme produces additional nonphysical forces and the solution is not acceptable. And last, in the on-land tsunami propagation the dry/wet situation is a critical point. Here both the water height h and the mass flow $q = hu$ converge to zero while the velocity u does not vanish. Accurate approximations where $h \ll \Delta x$ (let us say $h < \Delta x/100$), Δx being the characteristic length of the cell, turn out to be difficult since the numerical diffusion becomes the most prominent contribution. It means that the velocity may be unbounded close to the dry zone (and diverges to infinity in some cases) leading to a too small time step deriving from the CFL condition. Moreover, the finite volume method is powered with the MUSCL technique (monotonic upwind conservative schemes [*van Leer*, 1974] and see the book of *LeVeque* [2002] for an overview of the method) to improve the scheme accuracy with a very low additional computational cost.

The aim of this paper is twofold.

1. The presentation of a fully detailed numerical scheme, based on recent methods developed in the mathematical community for the shallow water system, including the nonconservative term with a special attention to the tsunami propagation problem. All the stages of the scheme are presented: the generic finite volume framework, the MUSCL technique, the *C*-property leading to the construction of the nonconservative fluxes, and, at last, the hydrostatic reconstruction to deal with the dry/wet situations.
2. The verification and validation of the numerical code, using synthetic, laboratorial, and field benchmarks. The synthetic and the experimental benchmarks that we adopt were used by *Synolakis et al*. [2008] and *Tinti and Tonini* [2013], extracted from the Long-Wave Run-Up Models Workshops, editions 1, 2 and 3 [*Liu et al*., 1990; *Yeh et al*., 1996; *Synolakis and Bernard*, 2006]. This synthetic validation process, including analytical and laboratorial benchmarks, aims to assess the robustness and the accuracy of the method.

For a complementary code validation, we use an historical tsunami event. The 28 February 1969 event was a submarine earthquake Ms7.9, with epicenter located on the Horseshoe Abyssal Plain, south-east of the Gorringe bank, approximately the same location as the noticeable 1755 Lisbon earthquake and tsunami. The earthquake struck western Portugal and Morocco at 02:40:32.5 UTC and a small tsunami was recorded in tide stations of mainland Portugal, Azores archipelago, Spain, and Morocco [*Baptista et al*., 1992]. The tsunami records were analyzed by *Baptista et al*. [1992]. Later, *Heinrich et al*. [1994] and *Gjevik et al*. [1997] presented numerical simulations of the tsunami propagation along the Portuguese coastline and in the Tagus estuary.

We perform multiple simulations of the 1969 tsunami, considering two different aspects: the open-sea and the inside of Tagus estuary propagation. The numerical code is able to reproduce the recorded waveforms for both cases, even with the complex bathymetry and reflective characteristics of the Tagus estuary.

2. Model and Numerical Scheme

Tsunami modeling involves the shallow water system modified with nonconservative terms such as the bathymetry effect, the friction, and/or the turbulence. We skip the two last terms since we focus on the bathymetry term and its numerical treatment. The system writes

$$\partial_t h+\partial_x(hu)+\partial_y(hv)=0, \tag{1}$$

$$\partial_t(hu)+\partial_x\left(hu^2+\frac{g}{2}h^2\right)+\partial_y(huv)=-gh\partial_x b, \tag{2}$$

$$\partial_t(hv)+\partial_x(huv)+\partial_y\left(hv^2+\frac{g}{2}h^2\right)=-gh\partial_y b, \tag{3}$$

where h denotes the water height, (u, v) the fluid velocity vector with components along the x and y axis, b the bathymetry, and $g=9.81\ \mathrm{m/s^2}$ the gravitational acceleration. Moreover, $\eta = h + b$ is the free surface, and vector $W = (h, hu, hv)$ combines the conservative quantities while $V = (h, u, v, b)$ corresponds to the physical variables vector.

2.1. Mesh and Notations

Let $\Omega_x=[0,L]$ with L a positive real number. We define the cells $c_{i\cdot}=[x_{i-1/2}, x_{i+1/2}]$ with interfaces $x_{i+1/2}=i\Delta x$, $x_{i-1/2}=x_{i+1/2}-\Delta x$ and center $x_i=\frac{x_{i-1/2}+x_{i+1/2}}{2}$, $i=1,\cdots,I$, where we have set $\Delta x = L/I$. In the same way, the cells $c_{\cdot j}=[y_{j-1/2}, y_{j+1/2}]$ represent a partition of $\Omega_y=[0,H]$, $H>0$ with interfaces $y_{j+1/2}=j\Delta y$, $y_{j-1/2}=y_{j+1/2}-\Delta y$ and center $y_j=\frac{y_{j-1/2}+y_{j+1/2}}{2}$, $j=1,\cdots,J$ with $\Delta y = H/J$.

Domain $\Omega=[0,L]\times[0,H]$ is decomposed into nonoverlapping $I \times J$ cells $c_{ij}=c_{i\cdot}\times c_{\cdot j}$, $i=1,\cdots,I$, $j=1,\cdots,J$, with centroid (x_i, y_j) and interfaces $e_{i+1/2,j}=\{x_{i+1/2}\}\times c_{\cdot j}$, $e_{i-1/2,j}=\{x_{i-1/2}\}\times c_{\cdot j}$, $e_{i,j+1/2}=c_{i\cdot}\times\{y_{j+1/2}\}$, $e_{i,j-1/2}=c_{i\cdot}\times\{y_{j-1/2}\}$. For a prescribed final time T, $0=t^0<t^1<\cdots<t^n<\cdots<t^N=T$ is a subdivision with nonconstant time step $\Delta t^n=t^{n+1}-t^n$ that will be adapted to satisfy the CFL condition.

Real number ϕ_{ij}^n represents an approximation of the mean value over cell c_{ij} for any function $\phi=h,\eta,b,u,v$ at time t^n. We recall that for regular functions over the cell c_{ij} (say C^2), the point-wise value at (x_i, y_j) is a second-order approximation of the mean value. We denote by $W_{ij}^n=(h_{ij}^n,(hu)_{ij}^n,(hv)_{ij}^n)$ the vector of the conservative variables and by $V_{ij}^n=(h_{ij}^n,u_{ij}^n,v_{ij}^n,b_{ij}^n)$ the vector of the physical variables where we have set

$$u_{ij}^n=\frac{(hu)_{ij}^n}{h_{ij}^n},\qquad v_{ij}^n=\frac{(hv)_{ij}^n}{h_{ij}^n},$$

when $h_{ij}^n>0$, and 0 otherwise. Real numbers $\phi_{i+1/2j,L}^n$ and $\phi_{i+1/2j,R}^n$ represent approximations on the left and right side of interface $e_{i+1/2j}$ while $\phi_{ij+1/2,L}^n$ and $\phi_{ij+1/2,R}^n$ stand for approximations on the lower and upper side of interface $e_{ij+1/2}$ (see Figure 1).

2.2. Nonconservative Problem and Well-Balanced Scheme

Due to the change of topography in space, the nonconservative term $-gh\nabla b$ is required to preserve some steady state configurations such as the water at rest, where the velocity is null and η is constant in the wet area. Indeed, writing the mass flow equation with zero velocity, the steady state assumption yields that the free surface η is constant and we have

$$\begin{aligned}\partial_t(hu)+\partial_x\left(hu^2+\frac{g}{2}h^2\right)+\partial_y(huv)&=gh\partial_x h\\&=gh\partial_x(\eta-b)\\&=-gh\partial_x b.\end{aligned}$$

The same property holds for the v component. Consequently, the nonconservative term $-gh\nabla b$ on the right-side compensates the hydrostatic pressure variation due to the bathymetry variations and the well-balanced property has to be mimicked at the discrete level. Discretization of the nonconservative term is still an important challenge to provide some nice properties such as stability and well-balancedness. For example, the simple discretization

$$-gh\partial_x b\approx -gh_{ij}\frac{b_{i+1,j}-b_{i-1,j}}{2\Delta x} \tag{4}$$

is not viable; such an approximation coupled with a classical numerical flux (Rusanov, HLL) will induce nonphysical motions, and after some steps the water moves alone, leading to a wrong simulation.

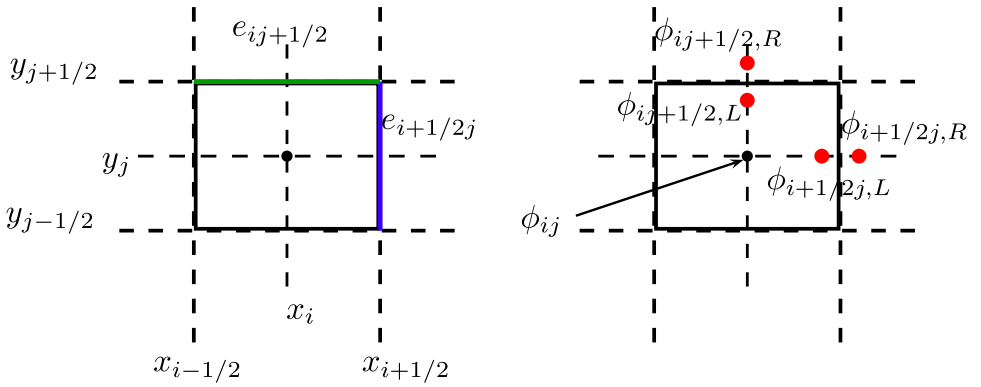

Figure 1. Notations and grid.

Consequently, preserving the water at rest configuration (the *C*-property) is the minimal requirement that the numerical scheme has to respect. A scheme is then said to be well-balanced (for the water at rest case) if it preserves this specific situation. Other types of steady state solution can also be preserved (the so-called moving water stationary solutions) and there exists a large literature on this subject in the mathematical community (we refer to *Delestre et al.* [2014] for an overview of the up-to-date techniques). Nevertheless, the water at rest is the main steady state that one has to preserve in the applications involving lakes or oceans.

To highlight the importance of such a property, we prove hereafter why expression (4) is not correct. Assume that the lake is at rest at time t^n, then we have $u_{ij}^n = v_{ij}^n = 0$ while $h_{ij}^n + b_{ij}^n = \eta_{ij}^n = \eta \in \mathbb{R}$. Computing the next time step for the velocity using the first-order finite volume scheme equipped with a viscous flux such as the Rusanov or the HLL one [see, e.g., *Toro*, 2009] leads to

$$
\begin{aligned}
h_{ij}^{n+1} u_{ij}^{n+1} &= -\frac{g\Delta t}{4\Delta x}\left((h_{i+1,j}^n)^2 - (h_{i-1,j}^n)^2\right) - \\
&\quad - h_{ij}^n \frac{b_{i+1,j}^n - b_{i-1,j}^n}{2\Delta x}\Delta t \\
&= -\frac{g\Delta t}{4\Delta x}(h_{i+1,j}^n - h_{i-1,j}^n)(h_{i+1,j}^n + h_{i-1,j}^n) - \\
&\quad - h_{ij}^n \frac{b_{i+1,j}^n - b_{i-1,j}^n}{2\Delta x}\Delta t \\
&= \frac{g\Delta t}{4\Delta x}(b_{i+1,j}^n - b_{i-1,j}^n)(h_{i+1,j}^n + h_{i-1,j}^n) - \\
&\quad - h_{ij}^n \frac{b_{i+1,j}^n - b_{i-1,j}^n}{2\Delta x}\Delta t \\
&= -g\Delta t \frac{b_{i+1,j}^n - b_{i-1,j}^n}{2\Delta x}\left(h_{ij}^n - \frac{h_{i+1,j}^n + h_{i-1,j}^n}{2}\right) \\
&= g\Delta t \frac{b_{i+1,j}^n - b_{i-1,j}^n}{2\Delta x}\left(b_{ij}^n - \frac{b_{i+1,j}^n + b_{i-1,j}^n}{2}\right) \\
&= g\Delta t \frac{b_{i+1,j}^n - b_{i-1,j}^n}{4\Delta x}(2b_{ij}^n - b_{i+1,j}^n + b_{i-1,j}^n).
\end{aligned}
$$

Clearly, the right-hand side does not vanish except for the particular case of a constant or linear bathymetry (affine strictly speaking). Hence, $h_{ij}^{n+1} u_{ij}^{n+1} \neq 0$. The steady state flow is no longer preserved and such a scheme leads to an erroneous evaluation of numerical approximations. On the other hand, we can check that if one employs the following discretization:

$$
-gh\partial_x b \approx -g\frac{h_{i+1,j}^n + h_{i-1,j}^n}{2} \cdot \frac{b_{i+1,j}^n - b_{i-1,j}^n}{2\Delta x},
$$

we obtain a well-balanced scheme for the water at rest situation since the velocity remains null. A major difficulty is that the choice of the discretization of the nonconservative term strongly depends on the discretization of the conservative part and the last choice turns out to be inadequate if, for example, we use the

Roe numerical flux [see, e.g., *Toro*, 2009]. Therefore, the nonconservative contribution has to be adapted to a function of the numerical flux used in the conservative term.

2.3. MUSCL Technique

The finite volume method is an excellent framework due to its built-in conservation property but it suffers of an important numerical diffusion if one uses first-order approximations. The MUSCL technique, initially developed by van Leer [*van Leer*, 1974], is a popular method to easily increase the accuracy while preserving the robustness. It is based on two steps: a local linear reconstruction to achieve the second-order, and a limiting procedure for preventing the solution from generating nonphysical oscillations.

To compute an approximation of the first derivative for any function $\phi = h, \eta, u, v, b$, we define the slopes for the x and y direction, respectively, with

$$p^n_{i+1/2j}(\phi) = \frac{\phi^n_{i+1j} - \phi^n_{ij}}{\Delta x}, \quad p^n_{ij+1/2}(\phi) = \frac{\phi^n_{ij+1} - \phi^n_{ij}}{\Delta y},$$

and one can achieve a more accurate approximation taking for example (see Figure 2)

$$\phi^n_{i-1/2j,R} = \phi^n_{ij} - \frac{p^n_{i+1/2j} + p^n_{i+1/2j}}{2}\frac{\Delta x}{2},$$

on the right side of edge $e_{i-1/2j}$, and

$$\phi^n_{i+1/2j,L} = \phi^n_{ij} + \frac{p^n_{i+1/2j} + p^n_{i+1/2j}}{2}\frac{\Delta x}{2},$$

on the left side of edge $e_{i+1/2j}$. Notice that we have skipped the reference to ϕ for the slopes p for the sake of simplicity.

Such a reconstruction will give rise to oscillations in the vicinity of a discontinuity due to the Gibbs phenomenon and a nonlinear limiting procedure has to be implemented to preserve the monotonicity in each direction. The traditional MUSCL approach consists in substituting the original slopes by a limited version $\pi(\alpha, \beta)$ depending on the left and right unlimited slope (α and β, respectively), such that some stability criterion is fulfilled. Classical limiter operators such as the minmod or the van Leer limiters are involved in the limiting process [*van Leer*, 1974]. The van Leer limiter will be used in all the numerical simulations.

Then we define the stabilized reconstructed values on the left and right side of the vertical interfaces with

$$\phi^n_{i+1/2j,L} = \phi^n_{ij} + \pi\left(p^n_{i-1/2j}, p^n_{i+1/2j}\right)\Delta x/2,$$
$$\phi^n_{i-1/2j,R} = \phi^n_{ij} - \pi\left(p^n_{i-1/2j}, p^n_{i+1/2j}\right)\Delta x/2,$$

while we set for the horizontal interfaces

$$\phi^n_{ij+1/2,L} = \phi^n_{ij} + \pi\left(p^n_{ij-1/2}, p^n_{ij+1/2}\right)\Delta y/2,$$
$$\phi^n_{ij-1/2,R} = \phi^n_{ij} - \pi\left(p^n_{ij-1/2}, p^n_{ij+1/2}\right)\Delta y/2.$$

Notice that $\phi^n_{i+1/2j,L}$ and $\phi^n_{i-1/2j,R}$ are (in general) different and that we recover the constant piecewise representation when $\pi = 0$ with $\phi^n_{i+1/2j,L} = \phi^n_{i-1/2j,R} = \phi^n_i$. Therefore, the first-order case is a possible outcome of the second-order one. In the following $W^n_{i+1/2j,L}$ stands for the reconstructed conservative vector on the left side of interface $e_{i+1/2,j}$ and $V^n_{i+1/2j,L}$ the corresponding vector using the physical variables.

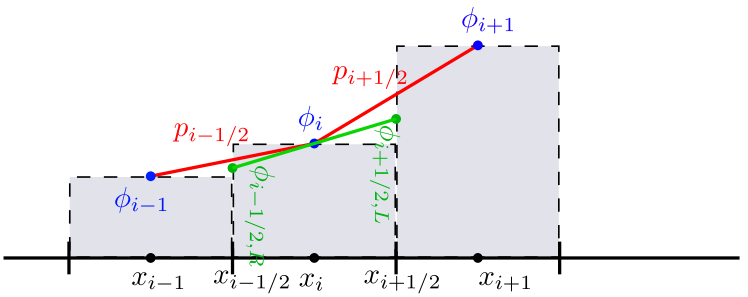

Figure 2. Slope and interface value reconstructions for the *Ox* direction. We skip the second index *j* for the sake of clarity.

An important point is that the reconstruction cannot be performed with h, η, and b at the same time for compatibility reasons. It has been

shown in *Audusse et al*. [2004] that a good choice is to first carry out the MUSCL procedure on h and η. Then we deduce the values for b setting (notice that the approximations of b now depend on time)

$$b^n_{i+1/2j,L}=\eta^n_{i+1/2j,L}-h^n_{i+1/2j,L},$$
$$b^n_{i-1/2j,R}=\eta^n_{i-1/2j,R}-h^n_{i-1/2j,R}.$$

We evaluate approximations $b^n_{ij+1/2,L}$ and $b^n_{ij-1/2,R}$ for the horizontal interfaces in the same way.

2.4. Hydrostatic Reconstruction

To design a discretization of the source term that preserves the C-property, we use the hydrostatic reconstruction proposed by *Audusse et al*. [2004], which allows to deal with complex flows with the dry/wet situation. In particular, such a technique preserves the positivity of the water height providing very good robustness and accuracy.

Consider a generic interface e and denote by b_L, h_L and b_R, h_R the bathymetry and water height for the left and right sides of the interface. We set $b^*=\max(b_L, b_R)$ and perform the hydrostatic reconstruction setting $h^*_L=\max(0, h_L-b^*+b_L)$, $h^*_R=\max(0, h_R-b^*+b_R)$. Therefore, h^*_L and h^*_R correspond to the water heights which are really involved in the pressure at the interface e. Figure 3 (left) shows that $h^*_R < h_R$ due to the step, the middle presents the dry/wet case where $h^*_L=h^*_R$, while the right gives an example of hydrostatic reconstruction with a piecewise linear bathymetry.

We now adapt the generic principle to a vertical interface $e_{i+1/2,j}$ for instance. We then denote by $b^{*,n}_{i+1/2j}=\max(b^n_{i+1/2j,L}, b^n_{i+1/2j,R})$, where $b^n_{i+1/2j,L}$ and $b^n_{i+1/2j,R}$ are approximations of topography on interface $e_{i+1/2,j}$, and set the new hydrostatic reconstruction variables

$$h^{*,n}_{i+1/2j,L}=\max(0, h^n_{i+1/2j,L}-b^{*,n}_{i+1/2j}+b^n_{i+1/2j,L}),$$
$$\eta^{*,n}_{i+1/2j,L}=h^{*,n}_{i+1/2j,L}+b^{*,n}_{i+1/2j},$$

with $h^n_{i+1/2j,L}$, $b^n_{i+1/2j,L}$ approximations of the water height and bathymetry on the left side of interface $e_{i+1/2,j}$. We proceed in the same way to compute $h^{*,n}_{i+1/2j,R}$ and $\eta^{*,n}_{i+1/2j,R}$. For the sake of consistency, we also use the notation $u^{*,n}_{i+1/2j,L}=u^n_{i+1/2j,L}$, $v^{*,n}_{i+1/2j,L}=v^n_{i+1/2j,L}$ and $u^{*,n}_{i+1/2j,R}=u^n_{i+1/2j,R}$, $v^{*,n}_{i+1/2j,R}=v^n_{i+1/2j,R}$ for the velocity.

We apply an identical algorithm for the horizontal interfaces of cell c_{ij} to evaluate $\phi^{*,n}_{i-1/2j,R}$, $\phi^{*,n}_{i-1/2j,R}$, $\phi^{*,n}_{ij+1/2,L}$, $\phi^{*,n}_{ij+1/2j,R}$, $\phi^{*,n}_{ij-1/2,L}$, $\phi^{*,n}_{ij-1/2j,R}$ for $\phi=h, \eta, u, v, b$. We shall denote by $W^{*,n}_{i-1/2,L}$ and $V^{*,n}_{i-1/2,L}$ the conservative and physical vectors after applying the hydrostatic reconstruction.

2.5. Numerical Fluxes and Source Term

The generic explicit finite volume scheme is

$$\begin{aligned} U^{n+1}_{ij}=U^n_{ij}-\frac{\Delta t}{\Delta x}\Big[&\mathcal{F}^n_{i+1/2j}+\varepsilon^n_{i+1/2j,L}\\ &-\mathcal{F}^n_{i-1/2j}-\varepsilon^n_{i-1/2j,R}\Big]\\ -\frac{\Delta t}{\Delta y}\big[&\mathcal{F}^n_{ij+1/2}+\varepsilon^n_{ij+1/2,L}\\ &-\mathcal{F}^n_{ij-1/2}-\varepsilon^n_{ij-1/2,R}\big]+\Delta t\mathcal{S}^n_{ij}, \end{aligned} \tag{5}$$

with $\mathcal{F}^n_{i-1/2j}=\mathbb{F}(W^{*,n}_{i-1/2j,L}, W^{*,n}_{i-1/2j,R}, v)$ a numerical flux for the conservative contribution that is cast in the viscous form

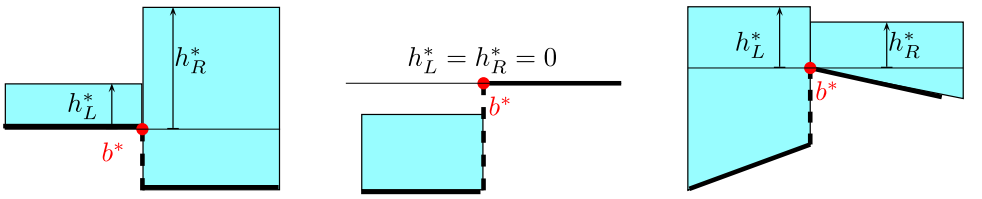

Figure 3. The hydrostatic static reconstruction: wet/wet with constant bathymetry (left), dry/wet case (middle), and wet/wet with linear bathymetry (right).

$$\mathbb{F}(W_L, W_R, \nu) = \frac{F(W_L, \nu) + F(W_R, \nu)}{2} - \lambda(W_R - W_L),$$

where

$$F(W, \nu) = \begin{pmatrix} hU \cdot \nu \\ huU \cdot \nu \\ hvU \cdot \nu \end{pmatrix} + \frac{gh^2}{2} \begin{pmatrix} 0 \\ \nu_x \\ \nu_y \end{pmatrix}$$

is the physical flux in the normal direction ν and $\lambda > 0$ is the scheme viscosity. In the following, the HLL numerical flux will be used in all the numerical simulations.

Function $\varepsilon^n_{i-1/2j,L} = \varepsilon(h^n_{i-1/2j,L}, h^{*,n}_{i-1/2j,L})$ is the nonconservative flux at edge $e_{i-1/2j}$ at the left side of the interface. We recall that for a nonflat bottom the nonconservativity yields

$$\varepsilon^n_{i-1/2j,L} + \varepsilon^n_{i-1/2j,R} \neq 0,$$

where this quantity represents the momentum variation due to the sharp change of topography at the interface. Of course, $\varepsilon^n_{i-1/2j,L} = \varepsilon^n_{i-1/2j,R} = 0$ if one has $b^n_{i-1/2j,L} = b^n_{i-1/2j,R}$, which corresponds to a local continuous bathymetry. We shall use the following discretization to deal with the discontinuous part of the nonconservative term

$$\varepsilon^n_{i+1/2j,L} = \frac{g}{2} \begin{pmatrix} 0 \\ (h^n_{i+1/2j,L})^2 - (h^{*,n}_{i+1/2j,L})^2 \\ 0 \end{pmatrix}$$

and similar expressions for the three other nonconservative contributions, namely $\varepsilon^n_{i-1/2j,R}$, $\varepsilon^n_{ij-1/2,L}$, and $\varepsilon^n_{ij+1/2,R}$, for the three other interfaces.

When dealing with the second-order approximation, the gradient of the bathymetry has to be substituted by its numerical representation corresponding to the regular part of the nonconservative term. Consequently, the contribution of the source term over the cell is

$$\mathcal{S}^n_{ij} = -g \begin{pmatrix} 0 \\ \dfrac{h^n_{i+1/2j,L} + h^n_{i-1/2j,R}}{2} \times \dfrac{b^n_{i+1/2j,L} - b^n_{i-1/2j,R}}{\Delta x} \\ \dfrac{h^n_{ij+1/2,L} + h^n_{ij-1/2,R}}{2} \times \dfrac{b^n_{ij+1/2,L} - b^n_{ij-1/2,R}}{\Delta y} \end{pmatrix}.$$

Notice that the source term for the cell does not involve the hydrostatic reconstructed variables but the original ones.

If one adopts a first-order scheme, we have $b^n_{i+1/2j,L} = b^n_{i-1/2j,R} = b_{ij}$. Hence, the source term in the cell vanishes and the contributions of the bathymetry variations are computed with the nonconservative flux. However, if the bathymetry is continuous and one employs a second-order scheme, the nonconservative flux deriving from the bathymetry discontinuity vanishes, and the change of topography contribution is exclusively computed with the source term in the cell S_{ij}. To sum up, both ε and S are computing the nonconservative term, but ε captures the sharp bathymetry variation at the interfaces, while S treats the smooth topography variations inside the cells.

2.6. Boundary Conditions

Edges $e_{I+1/2,j}$ are situated on the right boundary of the domain while $W_{I+1/2j,L}$ corresponds the reconstructed conservative vectors on the left side of these edges. One has to build a vector $W_{I+1/2j,R}$ for the right side following the prescription of the boundary condition. In the present study we shall consider two conditions:

Reflection condition. We set $h_{I+1/2j,R} = h_{I+1/2j,L}$, $b_{I+1/2j,R} = b_{I+1/2j,L}$, $u_{I+1/2j,R} = -u_{I+1/2j,L}$, and $v_{I+1/2j,R} = v_{I+1/2j,L}$.
Transmission condition. We set $h_{I+1/2j,R} = h_{I+1/2j,L}$, $b_{I+1/2j,R} = b_{I+1/2j,L}$, $u_{I+1/2j,R} = +u_{I+1/2j,L}$, and $v_{I+1/2j,R} = v_{I+1/2j,L}$.

We proceed in a similar way for sides $e_{1/2,j}$ on the left boundary and perform the same construction for the upper and the lower boundaries using $e_{i,J+1/2}$ and $e_{i,1/2}$, respectively. In the latter case, one has to modify the vertical component of the velocity v instead of u.

Notice that in both cases, the left and right values are equal or opposite, which means that for any function $\phi = h, hu$, one has $\nabla\phi \cdot n = 0$ at the boundary. Consequently, the gradient vanishes in the outward direction and the slopes are zero. Linear reconstructions are reduced to constant value functions, but second-order accuracy is preserved.

2.7. Full Second-Order Finite Volume Scheme

A second-order method in time is required to guarantee a global second-order method for smooth solutions. The usual RK2 (Heun method) is usually employed to be effective and robust. Assuming that we know all the vectors W_{ij}^n, $i=1,\cdots,I$, $j=1,\cdots,J$ at time t^n, we proceed in two substeps. We first compute a predicted approximation $W_{ij}^{n,1}$ for time $t^n+\Delta t$ applying successively the MUSCL procedure, the hydrostatic reconstruction, and the finite volume scheme (5). With $W_{ij}^{n,1}$ in hand, we proceed in the same way for computing a predicted approximation $W_{ij}^{n,2}$ for time $t^n+2\Delta t$. Then the Heun method consists in defining the corrected numerical solution

$$W_{ij}^{n+1} = \frac{1}{2} W_{ij}^{n} + \frac{1}{2} W_{ij}^{n,2},$$

which provides a second-order approximation in time at t^{n+1}. Numerical solution W_{ij}^{n+1} corresponds to a full second-order approximation both in space and time as long as we respect the CFL condition for the stability. In the following, the phrase "second-order scheme" corresponds to a global second-order both in space and time.

3. Numerical Tests and Validation

Several benchmarks are carried out to perform the verification and validation of the numerical scheme, through comparisons of the code predictions with analytical solutions, laboratory experiments and field measurements.

The validation stage guarantees that the numerical method correctly solves the equations where consistency, accuracy and stability are assessed with representative situations such as bathymetry change, dry/wet interface, and different boundary conditions.

To this end, three types of benchmark are considered: (1) the synthetic benchmark, where the numerical solution is compared to an analytical one; (2) the laboratory benchmark involving a confrontation of the numerical approximation with data deriving from laboratory experiences; and (3) a field benchmark, where we compare the numerical and the recorded results of a real event, the 1969 event that affected the coasts of Portugal, Spain, and Morocco.

The benchmarking process used to accomplish the geophysical component is an adaptation of the benchmark problems introduced by the Long-Wave Run-Up Models Workshops 1990 (Catalina Island in California), 1996 (Friday Harbor in Washington), and 2004 (Catalina Island) [*Liu et al.*, 1990; *Yeh et al.*, 1996; *Synolakis and Bernard*, 2006]. Later, as a product of these workshops, a technical memorandum was compiled by the National Oceanic and Atmospheric Administration [*Synolakis et al.*, 2007, 2008] and organized into four different categories: (1) basic hydrodynamic considerations, including the mass conservation and convergence; (2) analytical benchmarking, including the single wave on a simple beach problem; (3) laboratory benchmarking, including tests for a solitary wave on a simple beach, a solitary wave on a composite beach, a solitary wave on a conical island, tsunami run-up onto a complex 3-D beach (Monai Valley) and tsunami generation and run-up due to 3-D landslide; and (4) field benchmarking with the Rat Islands and the Okushiri tsunamis.

In our study, the basic hydrodynamic considerations are assessed to validate the numerical code. Mass conservation, convergence and stability are the major issues a code has to address. For nonconservative problems, the question of the well-balanced (or *C*-property) is also important, namely, some steady state situations have to be preserved. The most popular test is the so-called lake at rest configuration where a constant free surface with varying bathymetry and null velocity at $t = 0$ will be maintained for $t > 0$.

For the numerical code verification, we perform:

1. Three problems to test the run-up and inundation numerical solutions of the nonlinear shallow water equations based on *Synolakis et al*. [2008] and *Tinti and Tonini* [2013].
2. Three synthetic sanity check benchmarks, namely, tsunami run-up (without and with draw-down) on a slope plane beach benchmarks [*Carrier and Greenspan*, 1958; *Carrier et al*., 2003], and tsunami run-up of a planar surface oscillating in a paraboloidal basin benchmark [*Thacker*, 1981].
3. One laboratory benchmark due to the Monai, Okushiri tsunami that was carried out to compare the simulation with real experimental data in order to assess the validity of both the model and the numerical method.
4. One field benchmark comparing the recorded data of the 28 February 1969 North East Atlantic tsunami with the synthetic results of the numerical model.

3.1. Synthetic Benchmarks

Analytical benchmarking is a procedure that is used to identify the dependence of the results on the problem parameters [*Synolakis et al*., 2008; *Tinti and Tonini*, 2013].

3.1.1. Comparisons Between First- and Second-Order Methods

To assess and highlight the advantages of using a second-order method over a first-order one, we consider two classical analytical one-dimensional steady state benchmarks [see, e.g., *Delestre et al*., 2014], namely, a stationary transcritical flow without shock and a stationary transcritical flow involving a shock. The former case deals with a regular solution, allowing to assess the convergence differences between the first- and second-order technique, whereas the latter involves a discontinuous solution in order to check the ability to deal with shocks. In both cases, the ability to preserve the stationarity state with nonnull velocity is also addressed.

A channel with length L is discretized in space using a one-dimensional uniform mesh of I cells. Time step Δt is controlled by a CFL coefficient that we take equal to $CFL = 0.40$, i.e.,

$$\Delta t = CFL\frac{\Delta x}{\lambda},$$

with λ the maximum eigenvalue coefficient $|u|+\sqrt{gh}$ over all the states. Both flows have an upstream boundary located at $x = 0$ and the downstream one at $x = L$. The analytic equation governing such flows is given in *Delestre et al*. [2014] together with a wide set of analytic solutions for other 1-D and 2-D configurations. The configurations used in these two tests follow closely the corresponding benchmarks presented in the Delestre et al. compilation.

3.1.1.1. Regular Case

Since we are dealing with a smooth solution for both the free surface and the momentum, for the convergence studies we define the L^1- and L^∞-errors for a bounded L^1 function ϕ as

$$L^1-\text{error}: \frac{\sum_{i=1}^{I}|\phi_i^N-\phi_i^{ex}|}{I}$$

and

$$L^\infty-\text{error}: \max_{i=1,\dots,I}|\phi_i^N-\phi_i^{ex}|,$$

where $(\phi_i^{ex})_{i=1,\dots,I}$ and $(\phi_i^N)_{i=1,\dots,I}$ are, respectively, the exact and the approximated cell mean values at the final time $t^N = t_{\text{final}}$.

Notice that $hu = q_0$ is a constant since the solution does not depend on time and we carry out the simulations taking $L = 16$ m, $q_0 = 1.53$ m^2/s, while the bathymetry (bump) is given by

$$b(x) = \begin{cases} 0.2-0.05(x-6)^2 & , \quad 4\,\text{m} < x < 8\,\text{m}, \\ 0 & , \quad \text{otherwise}. \end{cases}$$

Under these conditions the flow is subcritical upstream with a Froude number close to 0.5 at $x = 0$ m and supercritical downstream with a Froude number around 1.9 at $x = L$. The regime transition occurs at the top of the bathymetry bump $x = 6$ m. Given the transcritical nature of the flow, the Dirichlet condition $hu = q_0$ is

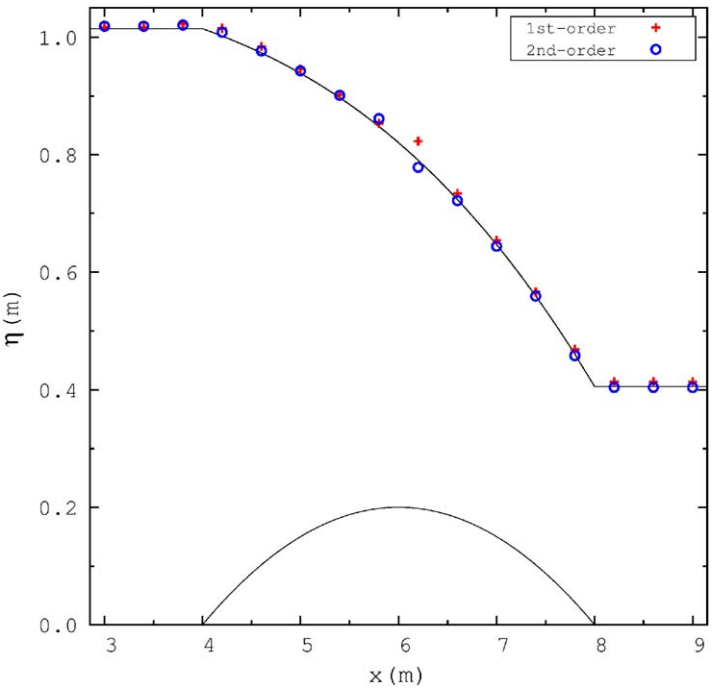

Figure 4. Free surface for the transcritical case without shock for $x \in [3\,\text{m}, 9\,\text{m}]$. The exact solution and bathymetry are presented together with the numerical solution obtained for a 40 cells mesh using the first- and second-order methods.

prescribed for $x = 0$ m and transmission conditions are considered for the outflow side. Computations are carried out, for different meshes, until the final time $t_{\text{final}} = 8$ s with the first- and the second-order versions of the code. The initial configuration corresponds to the exact solution of the shallow water system obtained numerically. Under these conditions, for $t = 8$ s the L^1- and L^∞-errors for both h and hu are several orders of magnitude higher than the corresponding variations of these variables between consecutive models, meaning that, in practice, a steady state regime has been reached.

The exact solution for both the free surface and the momentum is presented in Figures 4 and 5 where we plot the approximations for the free surface and the mass flow obtained using the two schemes being compared for the 40 cells mesh (290 time steps). For the sake of clarity the curves are plotted in the restricted interval [3 m, 9 m]. Errors for different mesh sizes and convergence rates for the free surface and the mass flow are provided in Tables 1 and 2, respectively.

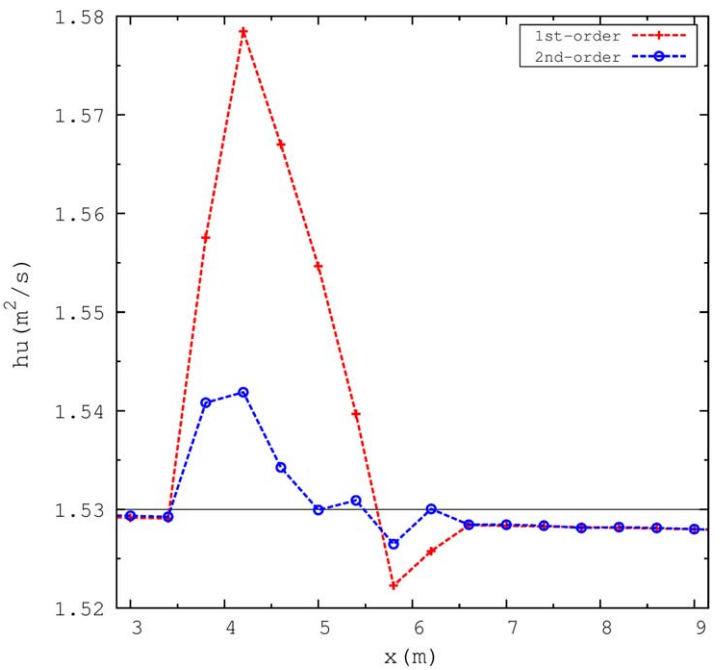

Figure 5. Momentum for the transcritical case without shock for $x \in [3\,\text{m}, 9\,\text{m}]$. The exact solution is shown together with the numerical solution obtained for a 40 cells mesh using the first- and second-order methods.

The simulation results presented in Figures 4 and 5 show that the second-order method provides a better qualitative approximation than the first-order one and a remarkable capacity to preserve the stationary momentum near the bump. The errors presented in Tables 1 and 2 highlight and clearly point out the error decreases that the second-order scheme can achieve. This is particularly noticeable for the L^1-error which is an indicator of the quality of the overall approximation with respect to the exact solution: L^1-errors are much lower in the second-order case and the order of convergence stays close to the optimal order (i.e., 2). The main reason preventing even better performance of the second-order scheme has to do with the fact that the first derivative of the

Table 1. Free Surface L^1 and L^∞-Errors (m) and Convergence Rates for the Transcritical Case Without Shock for the First- and Second-Order Methods

	First-Order Method				Second-Order Method			
Nb of Cells	err_1	Order	err_∞	Order	err_1	Order	err_∞	Order
80	3.68e-3		1.69e-2		1.38e-3		1.12e-2	
160	1.86e-3	1.1	8.62e-3	1.0	3.98e-4	1.8	6.22e-3	0.9
320	9.33e-4	1.0	4.36e-3	1.0	5.79e-5	2.8	1.97e-3	1.7
640	4.67e-4	1.0	2.20e-3	1.0	1.73e-5	1.7	9.89e-4	1.0
1280	2.33e-4	1.0	1.10e-3	1.0	4.89e-6	1.8	4.96e-4	1.0

bathymetry is not continuous at the beginning of the bump nor at its end. This leads to an order of convergence in the L^∞-norm limited to 1 for both methods.

3.1.1.2. Discontinuous Case

We turn now to the transcritical case with shock. In this case we take $L = 10$ m and the bathymetry is essentially the one used in the regular case, but shifted upstream

$$b(x) = \begin{cases} 0.2 - 0.05(x-5)^2 & , \quad 3\,\text{m} < x < 7\,\text{m}, \\ 0 & , \quad \text{otherwise.} \end{cases}$$

We set $hu = q_0 = 0.18$ m^2/s and $\eta(L) = 0.332$ m leading to a flow that is subcritical upstream, becomes supercritical at the top of the bump, remaining in this regime until a shock occurs before the end of the bump. From there on, the flow regime is subcritical again. Under these conditions one can show that the shock is located around $x = 6.65$ m. On the other hand, at $x = 0$ m the Froude number is approximately 0.2, being 2.7 just before the shock and 0.4 right afterward, reaching 0.3 downstream. Given the fact that the flow is subcritical both at $x = 0$ m and $x = L$, we adopt the boundary conditions: $hu(0) = q_0$ and $\eta(L) = 0.332$ m. The simulations are carried out until the final time $t_{\text{final}} = 20$ s to guarantee that the numerical solution has reached a steady state at the end of the simulation. As in the previous test case, the initial condition corresponds to the steady state exact solution.

Given the lack of smoothness of the solution, convergence analysis is not performed but we focus on the scheme capacity to capture the location and shape of the shock, as well as its ability to preserve the steady state. The exact solution for both the free surface and the mass flow is depicted in Figures 6 and 7, together with the corresponding numerical results obtained using the first- and second-order schemes for a 50 cells mesh (780 time steps). The curves are plotted in the interval $[2\text{ m},\ 8\text{ m}]$ for the sake of clarity. The approximation obtained with the second-order method is qualitatively closer to the exact solution, exhibiting a sharper shock and a momentum profile that is closer to the constant mass flow. The first-order method presents a higher diffusion profile where the shock capture is clearly less accomplished. Furthermore, we observe a severe deviation of hu with respect to the default constant mass flow value near the shock (and the bumps end) as well as in the vicinity of the beginning of the bump.

To highlight the importance of the limiting procedure, we also consider a simulation using the second-order reconstruction without the limiting procedure. Figure 8 presents the numerical results obtained for the free surface using the second-order method with and without limiter ("nl" for nonlimited) with a 100 cells mesh. In the nonlimited case, the free surface close to the shock discontinuity is quite inconsistent and

Table 2. Momentum L^1 and L^∞-Errors (m^2/s) and Convergence Rates for the Transcritical Case Without Shock for the First- and Second-Order Methods

	First-Order Method				Second-Order Method			
Nb of Cells	err_1	Order	err_∞	Order	err_1	Order	err_∞	Order
80	2.89e-3		2.70e-2		6.74e-4		6.30e-3	
160	1.42e-3	1.0	1.42e-2	0.9	2.13e-4	1.7	3.16e-3	1.0
320	6.98e-4	1.0	7.27e-3	1.0	5.15e-5	2.0	1.56e-3	1.0
640	3.43e-4	1.0	3.68e-3	1.0	1.48e-5	1.8	7.94e-4	1.0
1280	1.70e-4	1.0	1.85e-3	1.0	4.20e-6	1.8	4.02e-4	1.0

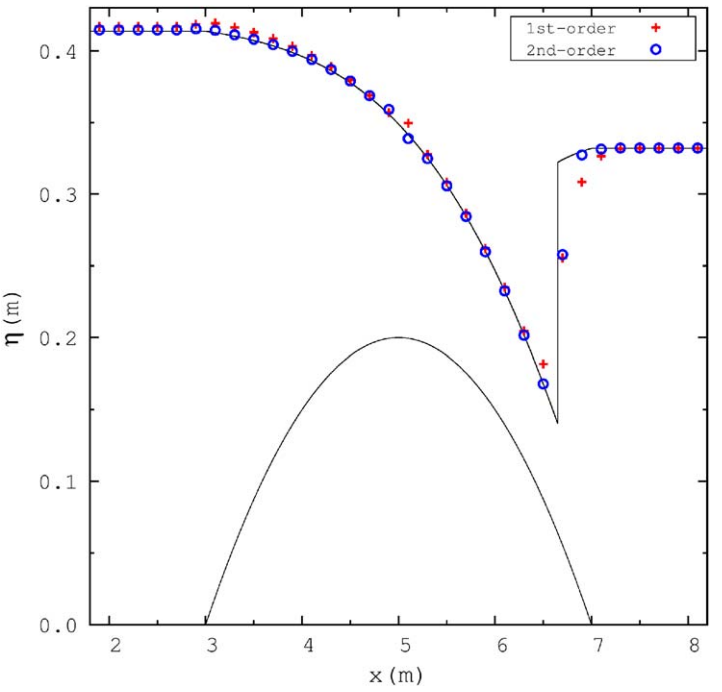

Figure 6. Free surface for the transcritical case with shock for $x \in [2\,\text{m}, 8\,\text{m}]$. The exact solution and bathymetry are presented together with the numerical solution obtained for a 50 cells mesh using the first- and second-order methods.

shows nonphysical oscillations, underlining the fundamental role of the limiting procedure when the solution is not smooth.

3.1.2. Tsunami Run-Up Onto a Sloping Plane Beach

The uniformly sloping beach benchmark consists of the comparison between the numerical solution obtained for the traveling and subsequent run-up of a leading depression N-wave (initial profile) across a 1/10 slope beach with the solution obtained by the analytical integral formula given in *Carrier and Greenspan* [1958] and *Carrier et al.* [2003]. In Figure 9 we depict the initial wave profile (see, e.g., *Carrier and Greenspan* [1958] for a complete description of the problem geometry). The goal of the benchmark, as described in *Synolakis et al.* [2008], is to compute the numerical approximations of the free surface and velocity at time $t=160$ s, $t=175$ s and $t=220$ s, and to compare them with the exact solution. We plot in Figure 10 the free surface using the first-order (left) and the second-order method (right) for the three times while Figure 11 displays the velocity. We qualitatively observe the convergence of the approximation as Δx decreases and report that the second-order clearly provides the best solution.

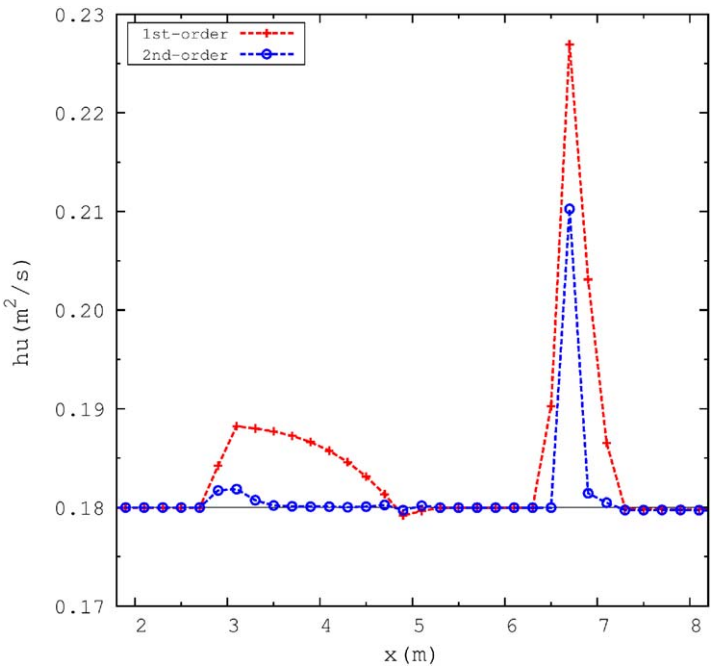

Figure 7. Momentum for the transcritical case with shock for $x \in [2\,\text{m}, 8\,\text{m}]$. The exact solution is shown together with the numerical solution obtained for a 50 cells mesh using the first- and second-order methods.

To quantify the impact of the second-order method, we report in Table 3 the error between the free surface minimum at $t=175$ s and the exact minimum (equal to -21.34) to determine the convergence orders. As expected, the second-order scheme provides the smallest errors and the convergence rate is around 1.6, whereas the first-order method provides the worst approximation to the exact solution. Note that the dry-wet interface is not well collocated since its position depends on whether a cell is wet or dry. We identify this issue as the major problem for obtaining an accurate solution and it is the main limiting factor of the numerical scheme. Effective second-order error cannot

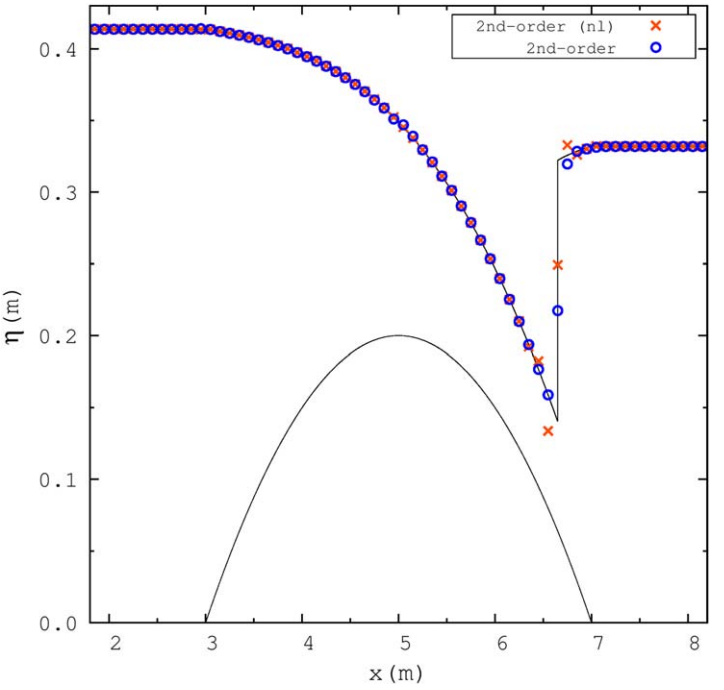

Figure 8. Free surface for the transcritical case with shock for $x \in [2\,\text{m}, 8\,\text{m}]$. Comparison between the numerical results obtained with the second-order method and a version of this method without limiter (nl) for a 100 cells mesh.

be achieved due to this important restriction and a better location of the dry/wet interface inside the cell is a crucial challenge.

3.1.3. Shoreline Position and Velocity

In this benchmark, the position and the velocity of the shoreline are compared with the ones given by semianalytical solutions of the nonlinear shallow water equations for an uniform sloping beach as given by *Carrier et al*. [2003].

To this end, we carry out the computation of the numerical solution obtained with the first- and the second-order method and compare them with the results of *Carrier et al*. [2003] for the run-up and run-down of a leading depression N-wave (typically caused by a seismic fault dislocation by subduction earthquake) on a plane beach with slope $\alpha = 1/200$. The initial condition assumes zero velocity everywhere and an initial vertical departure of the free surface with respect to the constant still water level η_{swl} such that

$$\eta_0(x) - \eta_{swl} = \alpha l \left(2ae^{-k(x-x_1)^2/l^2} - ae^{-k(x-x_2)^2/l^2} \right),$$

where x stands for the horizontal coordinate, which is zero at the quiescent position of the shoreline and points shoreward [see, e.g., *Carrier and Greenspan*, 1958], $l = 75$ km as suggested in *Carrier et al*. [2003], yielding $\alpha l = 375$ m, and

$$a = 0.01, \quad k = 3.5,$$
$$x_1 = -117178.5\,\text{m},$$
$$x_2 = -75000\,\text{m}.$$

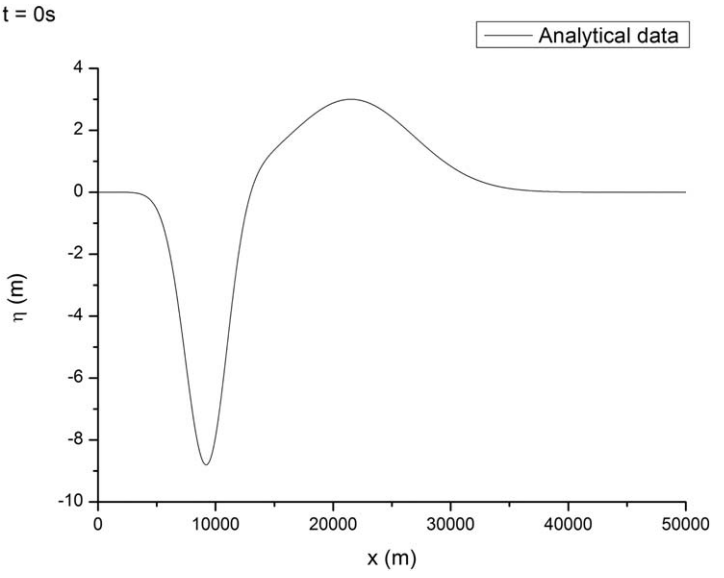

Figure 9. Initial free surface for the leading depression N-wave (run-up onto a sloping plane beach benchmark). The quiescent position of the shoreline and beach correspond, respectively, to $x = 0$ and $x < 0$).

The initial wave profile is depicted in Figure 12. The simulation is performed for different uniform meshes covering a 300 km domain until the final time $t_{\text{final}} = 5000$ s. In the simulations the water cutoff level to enforce cell drying is equal to 10^{-4} independently of the mesh size.

Table 4 presents, for different meshes, the run-up and run-down extreme positions, as well as the maximum inshore and offshore velocities, obtained with the second-order method, which we compare with the

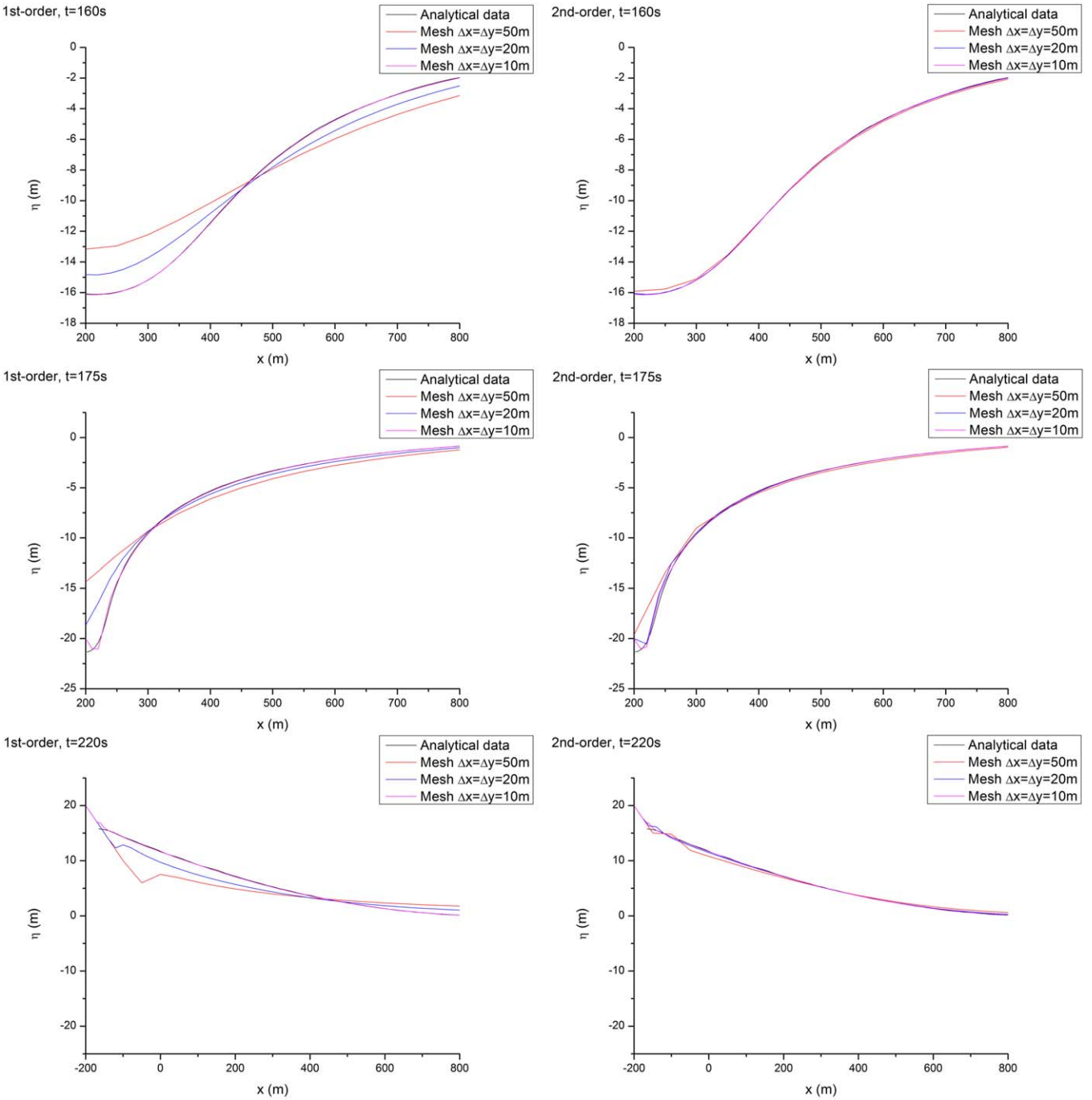

Figure 10. Free surface at $t = 160$ s (top), $t = 175$ s (middle), and $t = 220$ s (bottom) for the run-up on linear ramp. The left figure corresponds to the first-order scheme and the right figure to the second-order scheme.

exact values. We also indicate the corresponding time at which these events occur. Figure 13 depicts the shoreline position x_s as a function of time for the finest mesh for both the first- and the second-order methods. For the second-order method we observe, in the case of the finest mesh, good agreement for both the run-up and run-down extreme values, with an error smaller than 1.5 and 0.7%, respectively. The inshore maximum velocity is particularly well reproduced. The maximum offshore velocity, which occurs near the end of the run-down, is less accomplished, the overestimation pointing again to the need of a more accurate location of the dry/wet interface. The values of time at which these extreme events take place are in

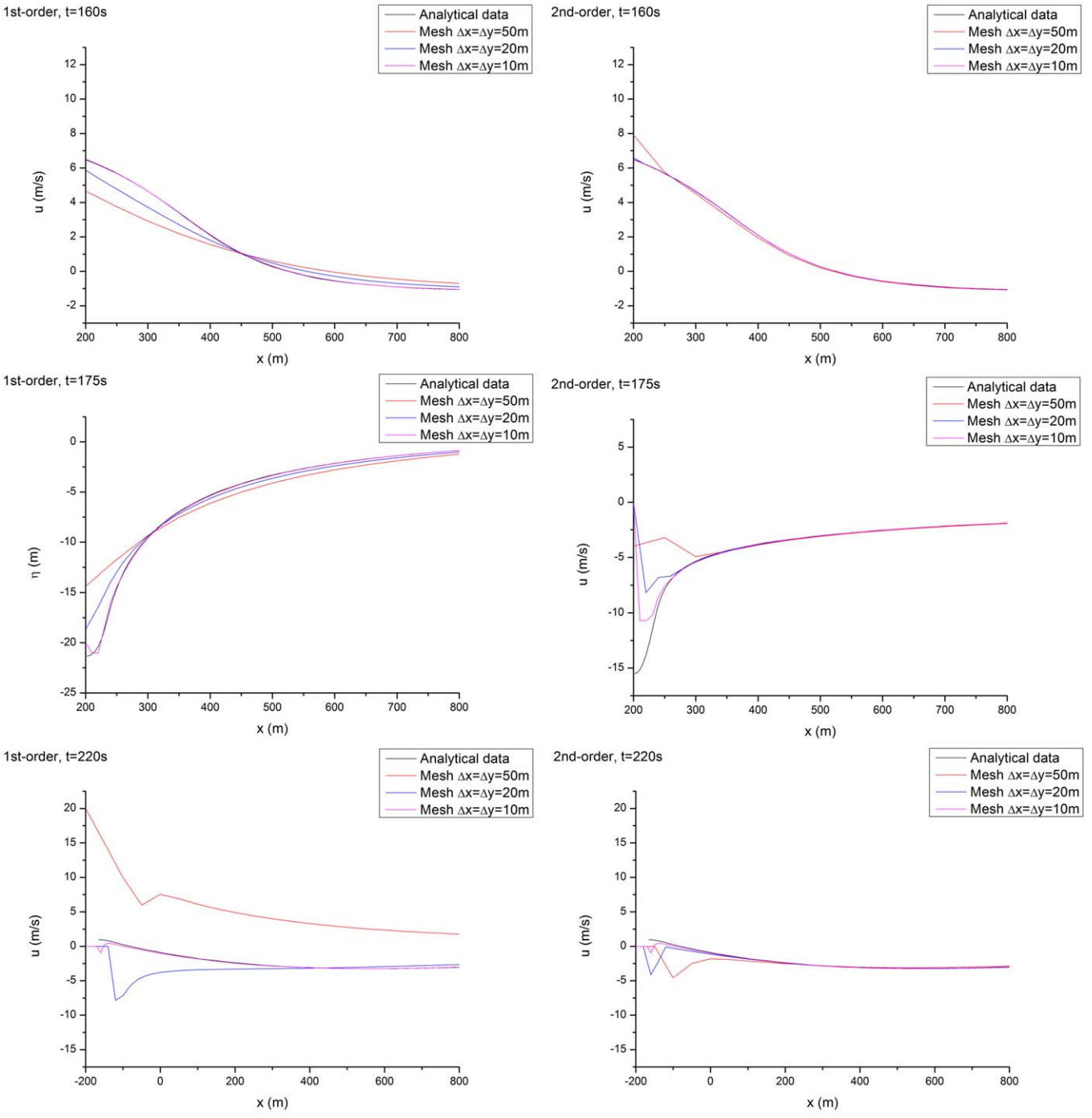

Figure 11. Water velocity at $t = 160$ s (top), $t = 175$ s (middle), and $t = 220$ s (bottom) for the run-up on linear ramp. The left figure corresponds to the first-order scheme and the right figure to the second-order scheme.

Table 3. Errors and Convergence Rates for the Free Surface Minimum (m) at Time $t = 175$ s

$\Delta x(m)$	Error First-Order	Order	Error Second-Order	Order
50	7.30		4.00	
20	3.22	0.9	0.98	1.5
10	1.25	1.3	0.31	1.7
5	0.58	1.1	0.10	1.6

good agreement with the exact results presented in *Carrier et al.* [2003, Figures 12c and 14]. The first-order method clearly fails to reproduce the run-down, even for a rather fine mesh, for both the position (see 13) and the velocity (not shown),

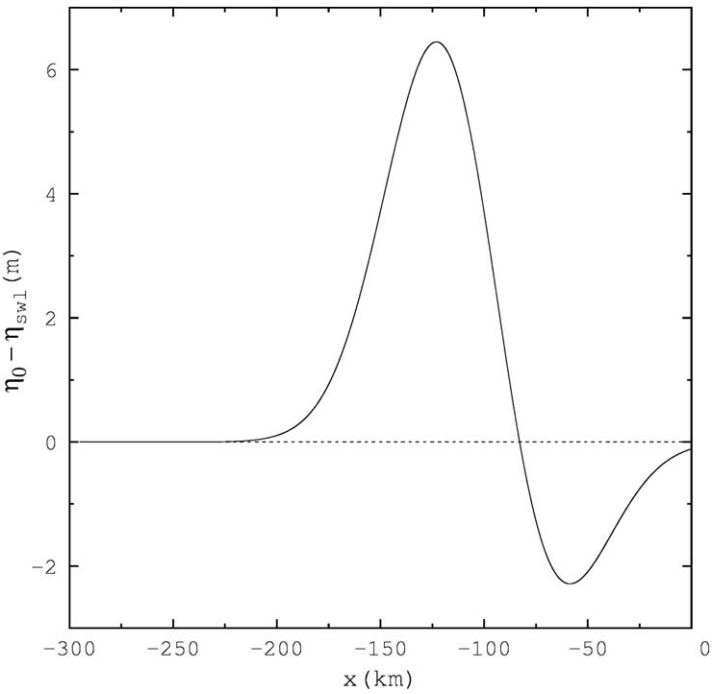

Figure 12. Initial vertical departure of the free surface with respect to the constant still water level for the leading depression N-wave (run-up/draw-down benchmark). The quiescent position of the shoreline corresponds to $x = 0$ and the beach to negative values of x).

highlighting the limitations of the method.

3.1.4. Tsunami Run-Up of a Planar Surface Oscillating in a Paraboloidal Basin

We now tackle a benchmark deriving from an analytical solution proposed by *Thacker* [1981] for a parabolic basin. This benchmark has been used by *Tinti and Tonini* [2013] to check the numerical schemes.

The computational domain is an ellipse of semiaxes L and l while the bathymetry is a paraboloid of equation [see *Brodtkorb et al.*, 2012, Figure 7, p. 11]

$$b(x,y)=b_0\left(1-\frac{x^2}{L^2}-\frac{y^2}{l^2}\right).$$

The initial free surface is a sloped plane following the horizontal axis. Due to the gravity force, the free surface is a plane that oscillates along the time around the perpendicular axis while the velocity component v remains null.

The exact solution has an analytical expression given by

$$\eta(x,y,t)=2A\frac{b_0}{L}\cos(\omega t)\left(\frac{x}{L}-\frac{A}{2L}\cos(\omega t)\right),$$

for the free surface and

$$u(x,y,t)=A\omega\,\sin(\omega t),\quad v(x,y,t)=0,\quad \omega=\sqrt{\frac{2gb_0}{L^2}}$$

for the velocity, where A is a free parameter that we shall set with the initial conditions. In numerical simulations we use $L=4700$ m, $l=1300$ m, $b_0=201.42$ m, and $A=235$m, leading to $\omega=1.3368\,10^{-2}$ s^{-1} and $T=470$ s.

By construction, η is a constant value at time $t=T/4$ and $t=3T/4$. Then, an easy way to check the code is assessing the flatness defaults by computing the difference between the maximum and the minimum

Table 4. Comparison Between Numerical (Second-Order) and Exact Extreme Values for the Run-Up and Run-Down (m), Inshore Velocity, and Offshore Velocity (m/s), for the Leading Depression N-Wave[a]

Nb of Cells	Max. Run-Up	Max. Run-Down	Max. Inshore Vel.	Max. Offshore Vel.
24,000	4,325	−1,788	10.55	−15.62
	(t = 2,963)	(t = 3,732)	(t = 2,554)	(t = 3,652)
37,500	4,320	−1,784	10.29	−15.25
	(t = 2,966)	(t = 3,730)	(t = 2,540)	(t = 3,646)
56,250	4,311	−1,776	10.09	−14.98
	(t = 2,960)	(t = 3,725)	(t = 2,521)	(t = 3,644)
84,375	4,313	−1,774	9.92	−14.76
	(t = 2,984)	(t = 3,725)	(t = 2,504)	(t = 3,643)
Exact solution	4,373	−1,763	9.91	−13.71

[a]The values of time (s) corresponding to these extreme values are also presented.

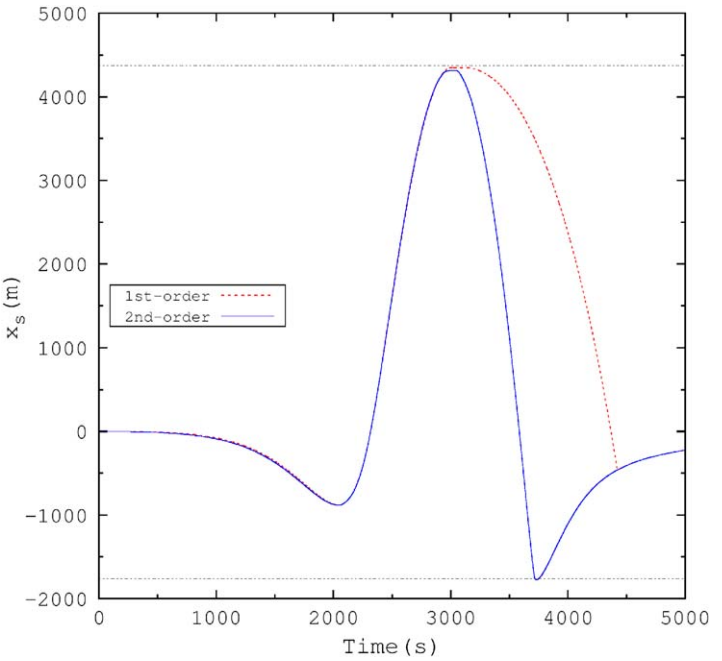

Figure 13. Numerical results obtained with the first- and second-order methods using the finest mesh for the temporal variation of the shoreline position x_s for the leading depression N-wave. The dotted horizontal lines represent the exact extreme values.

values of η at $t = 3T/4$. We carry out three simulations using meshes $M_1 = 250 \times 75$, $M_2 = 500 \times 150$, and $M_3 = 1000 \times 300$. In Table 5 we report the deviation with respect to the flatness default Δ_f.

Figure 14 displays the free surface of the basin at time $t = 3T/4$ corresponding to the flat situation where the exact solution is given by $\eta = 0$. We then visualize the two-dimensional errors distribution where the maximum and minimum are given in the caption. We obtain an almost constant zero-surface with respect to the characteristic length of the basin and no spurious oscillations are reported. The values in Table 5 correspond to the L^∞-norm of the error of the numerical approximation with respect to the exact solution. The free-surface error is of order $O(h)$ when using the first-order scheme while we recover full second-order with the MUSCL technique. Moreover, the MUSCL method does not produce any spurious oscillations and the free-surface flatness is almost preserved.

3.2. Laboratory Benchmark: Monai

The laboratory benchmark is an 1/400 scale laboratory experiment of the extreme Monai run-up which occurred as a consequence of the 1993 Okushiri tsunami (village of Monai in Okushiri Island, 1993 [*Matsuyama and Tanaka*, 2001]). Laboratory measurements were performed in a tank 205 m long, 6 m deep, and 3.4 m wide and three Points of Interest (PoI's) were considered, simulating virtual tide gauges. These PoI's are located at: (1) tide gauge 1: 4.521 m; 1.196 m; (2) tide gauge 2: 4.521 m; 1.696 m; and (3) tide gauge 3: 4.521 m; 2.196 m.

We carry out two simulations using the first-order and the second-order version of the code, the results being displayed, respectively, in the top and bottom rows of Figure 15. The elevations correspond to time $t = 14$ s (left) and $t = 16$ s (right). The second-order method provides qualitative better approximations with a sharper front and a larger dry zone which result from a less diffusive scheme. For instance, in the right bottom picture, the waves structure close to the cliff is steeper while the corresponding discontinuities appear smoother in the right upper picture.

To better quantify the error between the laboratory data and the numerical approximations, we compare the water height measurement at the three locations and draw the associated numerical curves in Figure 16. We observe the good correspondence until 50 s. From then on, the shallow water model is not representative enough due to the lack of dispersive terms. The second-order scheme provides a better approximation, in particular smaller structures (local variations) are captured, whereas they do not appear when the first-order scheme is used.

Table 5. Flatness Defaults (m) at Time $t = 175$ s for Different Meshes and Scheme Orders

Mesh	Δ_f: First-Order	Δ_f: Second-Order
$\Delta x = 250$ m, $\Delta y = 75$ m	0.82	0.072
$\Delta x = 500$ m, $\Delta y = 150$ m	0.44	0.021
$\Delta x = 1000$ m, $\Delta y = 300$ m	0.21	0.006

3.3. Field Benchmark: 28 February 1969 Tsunami

The 28 February 1969 submarine earthquake had a magnitude Ms = 7.9, and its epicenter located on the Horseshoe fault (HSF), 36.01°N and 10.57°W (see Figure 17). Its source was

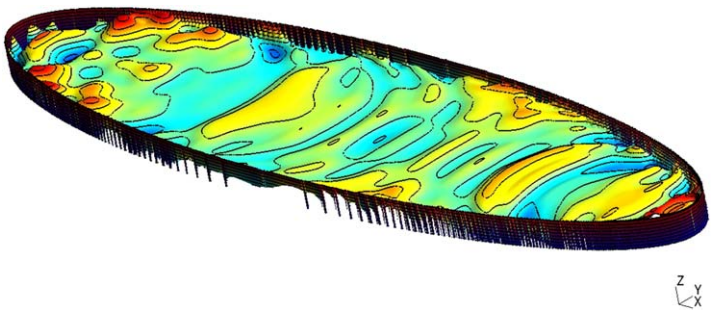

Figure 14. Free surface of the paraboloid basin at time $t = 3T/4$ corresponding to the exact solution $\eta = 0$ m. The free surface is situated between -0.003 m (blue) and 0.003 m (red) while the intermediate zero-level surface is yellow.

interpreted as a thrust fault with a small strike slip component [*Fukao*, 1973]. The earthquake generated a small tsunami that affected the coasts of Portugal, Spain, and Morocco [*Heinrich et al*., 1994; *Gjevik et al*., 1997]. The tsunami was recorded by several tide gauges, including the Cascais, Pedrouços, Terreiro do Paço, Cabo Ruivo and Lagos, in Portugal, and Casablanca, in Morocco. Figure 17 shows the epicenter of the 1969 earthquake and the location of several tide gauges where records are available, while Table 6 presents the tide gauges coordinates.

All tide records were digitized, linearly interpolated and detided to isolate the tsunami signal. To remove the tide we used a polynomial fitting of degree 9. The simulations were carried out for Mean Sea Level conditions. The bathymetric grid has a uniform spacing of 200 m, and was generated from the General Bathymetric Chart of the Oceans (GEBCO, http://www.gebco.net/).

To prescribe the initial conditions of the tsunami generation, we assume the earthquake rupture to be instantaneous and the water incompressible, so that the initial sea surface displacement mimics the coseismic deformation of the sea bottom. We adopt the fault plane parameter suggested by *Fukao* [1973]. The

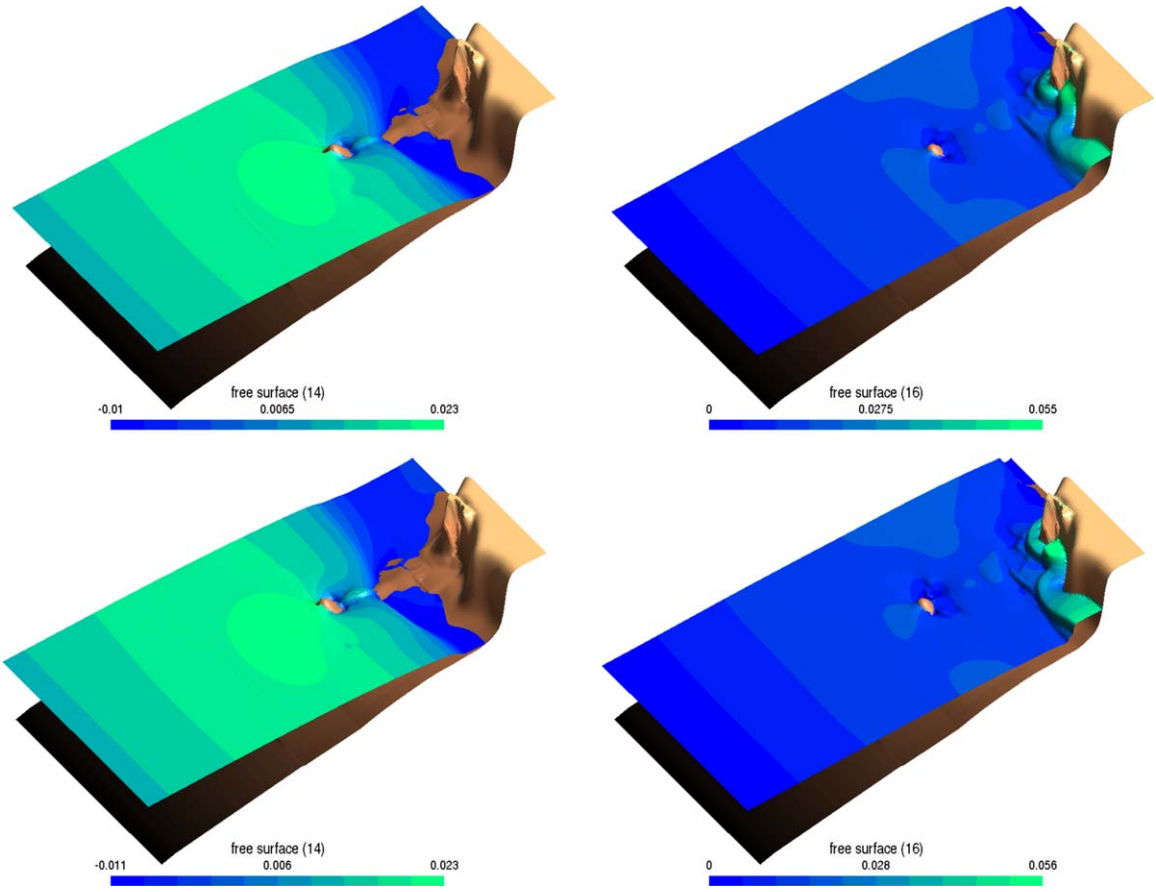

Figure 15. Comparison of the first- (top) and second-order (bottom) schemes at time $t = 14$ s (left) and $t = 16$ s (right).

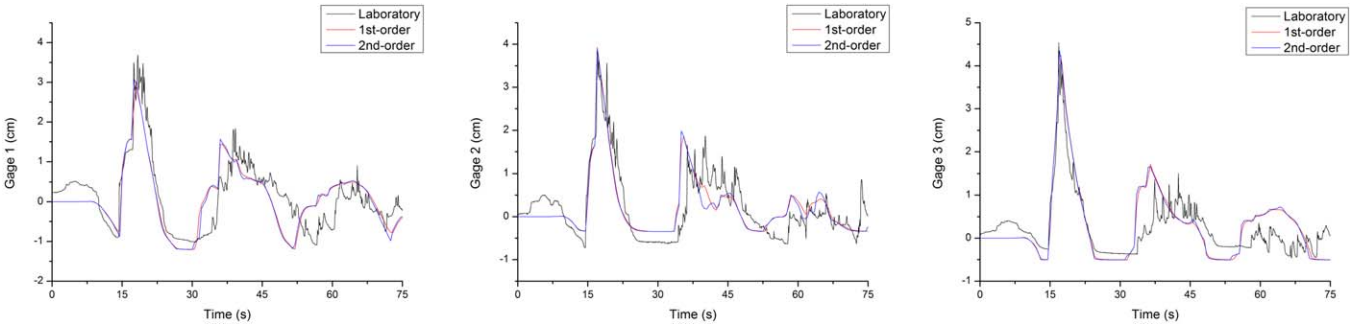

Figure 16. Comparison of laboratory and numerical data for three tide gauges located at points (4.521, 1.196) (tide gage 1), 4.521, 1.696 (tide gage 2), and 4.521, 2.196 (tide gage 3).

strike angle is 55°, the dip angle is 52°, and considering a seismic moment of $M_0 = 6.10^{20}$ Nm, the dimensions of the fault plane are fixed as 80 km long by 50 km wide [*Heinrich et al*., 1994]. To compute the coseismic deformation, we use the half-space elastic approach [*Okada*, 1985] implemented in Mirone suite [*Luis*, 2007].

The initial sea surface displacement is shown in Figure 18. The maximum vertical displacement is 1.65 m.

We carry out numerical simulations with the first- and the second-order method. Zero-velocity is assumed at the initial time. The initial time of the simulation, $t = 0$ s, is the time of the earthquake. We run the simulation until a final time of 180 min. Transmission conditions are prescribed on the whole boundary to make the waves freely flow out of the domain without spurious oscillations.

The comparison between the synthetic results and the recorded data focus on four aspects: (1) amplitude of the first wave; (2) arrival time of the tsunami first wave; (3) frequency of the first waves; and (4) first wave polarity.

3.3.1. Wave Amplitude

Figure 19 displays the comparison of the water elevation at the different locations with respect to the time, while Table 7 provides the maximum water height values for the recorded and simulated waves.

The main difficulty to fit the simulation with the recorded data is the grid size, which prevents representing structures smaller than 200 m and an accurate location of the sensors. We perform the simulations using

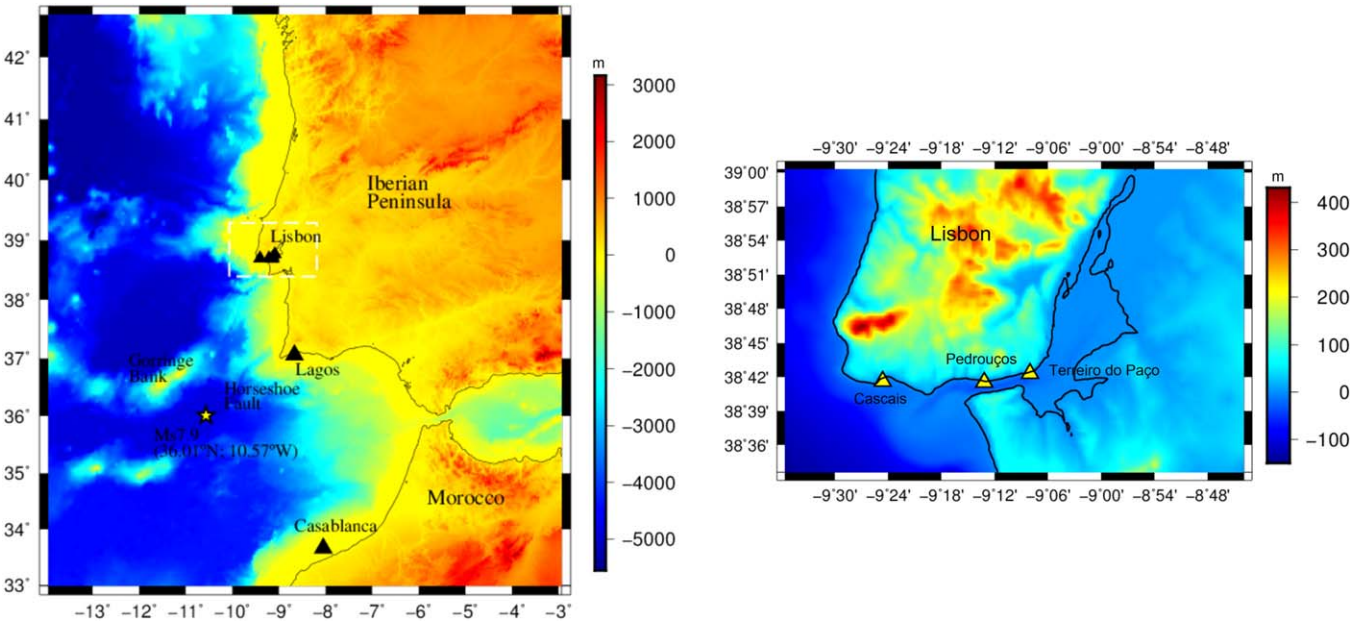

Figure 17. Location of Gorringe Bank. The epicenter of the 1969 earthquake near the Horseshoe fault is represented by a yellow star. The location of the tide gauge stations in Casablanca, Lagos, Cascais, and Tagus estuary are represented by triangles (left). Zoom of the Cascais and Tagus estuary tide stations location (right).

Table 6. Pol's Used in the 28 February 1969 Event With the Respective Location

	Location	
Station	Latitude (°N)	Longitude (°W)
Cascais	38.693	9.411
Pedrouços	38.690	9.259
Terreiro do Paço	38.704	9.136
Lagos	37.066	8.667
Casablanca	33.610	7.386

five virtual sensors as Points of Interest, each one situated in the neighbor cell of the real sensor localization, ensuring in this way that the synthetic waveforms are representative of the area. We focus on the three first tsunami waves since local geographical configurations produce new reflection waves that are later superposed on the waveform, and therefore are not well reproduced by the numerical simulations.

1. The Cascais PoI numerical waveform shows an amplitude about 11 and 29 cm larger than the observed waveform (46.7 cm), respectively, for the lower- and the higher-order method. Such differences may derive from the large diffusivity inherent to the first-order scheme which dramatically reduces the accuracy (a third of the water height). Since the gravitational wave is compressed and focused as the tsunami enters shallower water close to the coast, the high diffusion scheme is not able to correctly reproduce the energy concentration and provides erroneous estimates of the tsunami impact. The second-order scheme is, at least, accurate enough to give a relevant waveshape when it reaches the coast.
2. The Pedrouços tide gauge simulation shows, for the first-order scheme, an amplitude 10 cm smaller than the recorded one. In contrast, for the second-order scheme we observe an overestimation of about 6 cm.
3. The Terreiro do Paço comparison shows that the first wave peak amplitude is 19 and 43 cm, respectively, for the first- and the second-order methods. The recorded waveform shows an amplitude of 42 cm.
4. In Lagos, we achieve a good agreement between the amplitude of the recorded waveform and the simulation results. The first-order simulation presents a difference of 7 mm and the second-order one 8.4 cm.
5. The Casablanca second-order simulation, used mainly to analyze the polarity, shows differences of about 28 cm.

As a pattern, we observe that the first-order simulation results typically provide lower amplitude than the corresponding second-order results.

3.3.2. Tsunami Travel Time

Figure 19 displays the comparison of the tsunami arrival time. Table 8 provides the time for the recorded and simulated travel times.

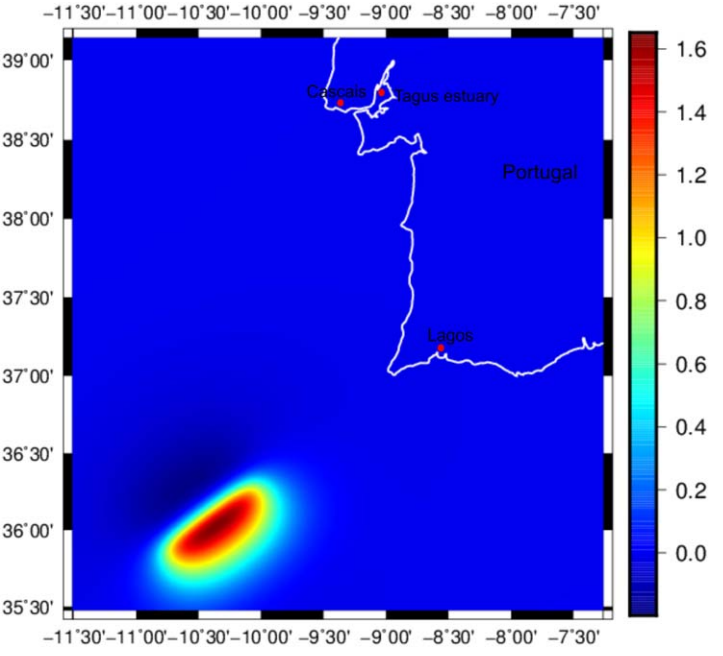

Figure 18. Initial deformation generated for the 1969 earthquake and location of the simulation PoI's in Portugal.

Tsunami travel times are generally well reproduced by the simulations, taking into account the tsunami propagation between the PoI and the real tide gauge.

1. The Cascais tide gauge recorded the peak of the first wave about 36 min after the earthquake while the first- and the second-order simulations present the arrival of the first wave 39 and 41 min after the earthquake, respectively.
2. The Pedrouços travel time is 66 min while the numerical simulations give travel times of 51 min, for both, first- and second-order.
3. The Terreiro do Paço observed travel time is 72.6 min while the simulation gives a travel time of 63 min for the first-order and 66 min for the second-order.

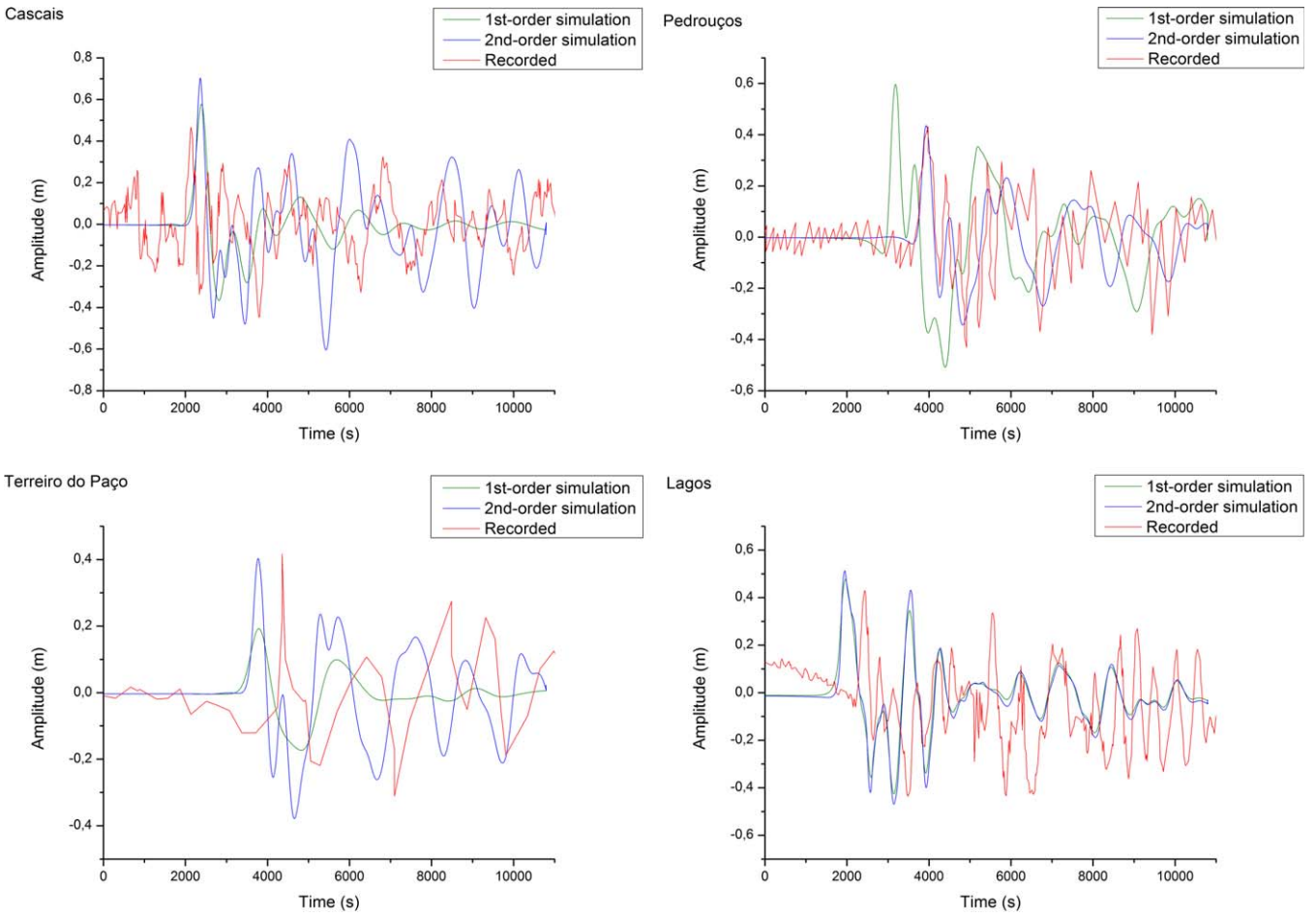

Figure 19. Tsunami waves amplitude for the Cascais, Pedrouços, Terreiro do Paço, Lagos, and Casablanca tide gauges. Comparison of the first- and second-order numerical simulation with the tide gauge waveform.

4. In Lagos Pol, the recorded travel time is 40.7 min while it is about 35 and 32 min, respectively, for the first- and the second-order scheme.
5. In Casablanca, the arrival time is not coherent with the recorded waveform (48 min in the recorded waveform and 32 min in the synthetic result obtained using the second-order simulation). This situation was already noted in previous studies [see, e.g., *Guesmia et al*., 1998].

In most cases, the numerical simulation provides earlier arrival times than the ones obtained from the recorded data. This is consistent with the bathymetric resolution and the very shallow area where the sensors are located, with a depth shallower than 2–4 m. The situation is particularly important for the tide gauges located on the shallow margins of the Tagus river. Nevertheless, the second-order simulations reproduce better the recorded waveforms, as expected.

Table 7. Amplitude: Comparison Between the Recorded Waveform and the Synthetic Results Obtained From First- and Second-Order Simulations

Station	Recorded (*m*)	First-Order (*m*)	Second-Order (*m*)
Cascais	0.467	0.577	0.759
Pedrouços	0.433	0.334	0.493
Terreiro do Paço	0.417	0.192	0.436
Lagos	0.429	0.436	0.513
Casablanca	0.212		0.476

3.3.3. Period

Tsunami propagation results into a series of waves due to the reflections and the refraction with the coast leading to a complex waveform constituted of the superposition of several frequencies. Nevertheless, one can observe that the lower frequency content is almost constant (at least for the three first periods) in all tide gauges, and mainly a function

Table 8. Arrival Time: Comparison Between the Recorded Waveform (Rec.) and the Synthetic Results Obtained With First- and Second-Order Simulations

Station	Rec. (s)	First-Order (s)	Second-Order (s)
Cascais	2136	2388	2494
Pedrouços	3978	3111	3194
Terreiro do Paço	4357	3788	3930
Lagos	2442	2099	1946
Casablanca	2892		1894

of the tsunami source size. To do a quantitative comparison we estimate the largest period by the delay between the first and the second peak and from the average of the three peaks for both observed and synthetic waveforms (see Figure 19).

1. The Cascais observed waveform is probably affected by the proximity with marine structures, resulting in three main superposed frequencies. It is possible to identify the high and low frequencies and perform the comparison with the simulated waveforms.
2. Pedrouços recorded waveform also shows a complex frequency content (see Figure 19). The numerical code reproduces fairly the lowest frequency.
3. In Terreiro do Paço, the period is better reproduced by the second-order simulation.
4. In Lagos, the recorded waveform has higher frequencies than all simulated waveforms.
5. In Casablanca, both observed and simulated periods are similar.

4. Conclusions

From the numerical point of view, the finite volume technique coupling the hydrostatic reconstruction and the second-order scheme MUSCL technique provides an efficient code with mass conservation and preserves an ocean at rest. Shocks are well represented and the MUSCL technique reduces the numerical diffusion and increases the accuracy without generating nonphysical oscillations. The code was submitted to three different types of benchmark to assess the accuracy, the robustness and the *C*-property. The benchmarks were performed with the first- and second-order schemes for the run-up, run-down and inundation numerical solutions of the nonlinear shallow water equations. Comparisons between the numerical and the real waveforms showed a very good agreement.

The model was tested with a realistic case, the propagation of the small tsunami generated by the 1969 tsunamigenic earthquake (Ms7.9) in the Tagus estuary. In spite of the complex bathymetry, the numerical code had a favorable performance and the comparison between numerical and recorded waveforms showed good agreement. As expected, the second-order scheme generates waveforms with a better approximation to the real waveforms recorded by the considered tide stations.

The main conclusions of this paper are:

1. The finite volume method is adequate for the numerical solution of the shallow water equations.
2. The implemented techniques increase the performance of the method.
3. Mathematical and geophysical benchmarks (analytical solutions, laboratory experiments and field measurements) validate the numerical code capability to simulate tsunami propagation, run-up and run-down with accuracy and robustness.

Future developments will include the introduction of a more recent limiting technique, namely the MOOD method, in place of the MUSCL method [*Figueiredo and Clain*, 2015], which provides effective second-order of accuracy and preserves some essential properties such as the positivity of the water height.

Acknowledgments
Historical data for Cascais and Lagos (1969 Lisbon Tsunami) are available at http://www. dgterritorio.pt/cartografia_e_geodesia/geodesia/redes_geodesicas/rede_maregrafica/. The tagus estuary data (typewriter document) are available at the Dom Luiz Institute library http://idl.ul.pt/node/33. This work is funded by the Portugal-France research agreement, through the research project GEONUM FCT-ANR/MAT-NAN/0122/2012. This research was financed by Portuguese Funds through FCT—Fundação para a Ciência e a Tecnologia, within the Project UID/MAT/00013/2013.

References

Audusse, E., F. Bouchut, M. O. Bristeau, R. Klein, and B. Perthame (2004), A fast and stable well-balanced scheme with hydrostatic reconstruction for shallow water flows, *SIAM J. Sci. Comput.*, *25*(6), 2050–2065.

Baptista, M. A., P. M. A. Miranda, and L. M. Victor (1992), Maximum entropy analysis of Portuguese tsunami data. The tsunamis of 28.02.1969 and 26.05.1975, *Sci. Tsunami Hazards*, *10*, 9–20.

Berger, M. J., D. L. George, R. J. LeVeque, and K. M. Mandli (2011), The GeoClaw software for depth-averaged flows with adaptive refinement. *Advances in Water Resources*, *34*, 1195–1206.

Bermúdez, A., and M. E. Vázquez (1994), Upwind methods for hyperbolic conservation laws with source terms, *Comput. Fluids*, *24*, 1049–1071.

Bermúdez, A., A. Dervieux, J. A. Desideri, and M. E. Vásquez (1998), Upwind schemes for the two-dimensional shallow water equations with variable depth using unstructured meshes, *Comput. Methods Appl. Mech. Eng.*, *155*, 49–72.

Berthon, C., and F. Fouchet (2012), Efficient well-balanced hydrostatic upwind schemes for shallow-water equations, *J. Comput. Phys.*, *231*, 4993–5015.
Brodtkorb, A. R., M. L. Saetra, and M. Altinakar (2012), Efficient shallow water simulations on GPUs: Implementation, visualization, verification, and validation, *Comput. Fluids*, *55*, 1–12.
Carrier, G. F., and H. P. Greenspan (1958), Water waves of finite amplitude on a sloping beach, *J. Fluid Mech.*, *4*, 97–109.
Carrier, G. F., T. T. Wu, and H. Yeh (2003), Tsunami run-up and draw-down on a plane beach, *J. Fluid Mech.*, *475*, 79–99.
Delestre, O., C. Lucas, P.-A. Ksinant, F. Darboux, C. Laguerre, T.-N.-T. Vo, F. James, and S. Cordier (2014), SWASHES: A compilation of shallow water analytic solutions for hydraulic and environmental studies, *Int. J. Numer. Meth. Fluids*, *74*, 229–230.
Duran, A., Q. Liang, and F. Marche (2013), On the well-balanced numerical discretization of shallow water equations on unstructured meshes, *J. Comput. Phys.*, *235*, 565–586.
Figueiredo, J., and S. Clain (2015), Second-order finite volume MOOD method for the shallow water with dry/wet interface, in *SYMCOMP 2015*, pp. 191–205, ECCOMAS, Portugal, Faro.
Fukao, Y. (1973), Thrust faulting at a lithospheric plate boundary the Portugal earthquake of 1969, *Earth Planet. Sci. Lett.*, *18*(2), 205–216.
Gallouët, T., J. M. Hérard, and N. Seguin (2003), Some approximate Godunov scheme to compute shallow-water equations with topography, *Comput. Fluids*, *32*, 479–513.
George, D. L. (2004), Numerical approximation of the nonlinear shallow water equations with topography and dry beds: A Godunov-type scheme, PhD thesis, Univ. of Washington, Seattle.
George, D. L., and R. J. LeVeque (2006), Finite volume methods and adaptive refinement for global tsunami propagation and local inundation, *Sci. Tsunami Hazards*, *24*, 319–328.
Gjevik, B., G. Pedersen, E. Dybesland, C. Harbitz, P. Miranda, M. A. Baptista, and M. Guesmia (1997), Modeling tsunamis from earthquake sources near Gorringe Bank southwest of Portugal, *J. Geophys. Res.*, *102*, 27,931–27,949.
Goto, C., Y. Ogawa, N. Shuto, and F. Imamura (1997), *IUGG/IOC time project: Numerical Method of Tsunami Simulation With the Leap-Frog Scheme*, Manuals and Guides 35, Intergovernmental Oceanographic Commission of UNESCO.
Greenberg, J. M., and A. Y. Leroux (1996), A well-balanced scheme for the numerical processing of source terms in hyperbolic equations, *SIAM J. Numer. Anal.*, *33*(1), 1–16.
Guesmia, M., P. H. Heinrich, and C. Mariotti (1998), Numerical simulation of the 1969 Portuguese tsunami by a finite element method, *Nat. Hazards*, *17*(1), 31–46.
Heinrich, P., M. A. Baptista, and P. Miranda (1994), Numerical simulation of the 1969 tsunami along the Portuguese coasts. Preliminary results, *Sci. Tsunami Hazards*, *12*(1), 3–23.
Hou, T., and P. LeFloch (1994), Why non-conservative schemes converge to the wrong solutions: Error analysis, *Math. Comput.*, *32*, 497–530.
Imamura, F., A. C. Yalciner, and G. Ozyurt (2006), *Tsunami Modelling Manual*, UNESCO IOC international training course on Tsunami Numerical Modeling.
LeVeque, R. J. (2002), *Finite Volume Methods for Hyperbolic Problems, Cambridge Texts Appl. Math*., Cambridge Univ. Press, Cambridge, U. K.
LeVeque, R. J., D. L. George, and M. J. Berger (2011), Tsunami modeling with adaptively refined finite volume methods, *Acta Numer.*, *20*, 211–289.
Liu, P. L. F., C. Synolakis, and H. Yeh (1990), A report on the international workshop on long wave runup, *J. Fluid Mech.*, *229*, 678–688.
Liu, P. F. L., S. B. Woo, and Y. S. Cho (1998), *Computer Programs for Tsunami Propagation and Inundation*, Cornell Univ., Ithaca, N. Y.
Luis, J. F. (2007), Mirone: A multi-purpose tool for exploring grid data, *Comput. Geosci.*, *33*(1), 31–41.
Matias, L. M., T. Cunha, A. Annunziato, M. A. Baptista, and F. Carrilho (2013), Tsunamigenic earthquakes in the Gulf of Cadiz: Fault model and recurrence, *Nat. Hazards Earth Syst. Sci.*, *13*, 1–13, doi:10.5194/nhess-13-1-2013.
Matsuyama, M., and H. Tanaka (2001), An experimental study of the highest run-up height in the 1993 Hokkaido Nansei-oki earthquake tsunami, paper presented at U.S. National Tsunami Hazard Mitigation Program Review and International Tsunami Symposium, ITS, Seattle, Wash.
Nikolos, I. K., and A. I. Delis (2009), An unstructured node-centered finite volume scheme for shallow water flows with wet/dry fronts over complex topography, *Comput. Methods Appl. Mech. Eng.*, *198*, 3723–3750.
Okada, Y. (1985) Surface deformation due to shear and tensile faults in a half-space, *Bull. Seismol. Soc. Am.*, *75*(4), 1135–1154.
Roberts, S., O. Nielsen, D. Gray, and J. Sexton (2010), *ANUGA User Manual*, Geosci. Aust. and Aust. Natl. Univ., Canberra.
Salah, A. M., E. J. Nelson, and G. P. Williams (2010), Tools and algorithms to link horizontal hydrologic and vertical hydrodynamic models and provide a stochastic modeling framework, *J. Adv. Model. Earth Syst.*, *2*, 1–14, doi:10.3894/JAMES.2010.2.12.
Synolakis, C. E., and E. N. Bernard (2006), Tsunami science before and beyond Boxing Day 2004, *Philos. Trans. R. Soc. A*, *364*, 2231–2265.
Synolakis, C. E., E. N. Bernard, V. V. Titov, U. Kânoğlu, and F. I. González (2007), NOAA Tech. Memo., OAR PMEL−*135*, NOAA/Pac. Mar. Environ. Lab., Seattle, Wash.
Synolakis, C. E., E. N. Bernard, V. V. Titov, U. Kânoğlu, and F. I. González (2008), Validation and verification of tsunami numerical models, *Pure Appl. Geophys.*, *165*, 2197–2228.
Thacker, W. C. (1981), Some exact solutions to the nonlinear shallow-water wave equations, *J. Fluid Mech.*, *107*, 499–508.
Tinti, S., and R. Tonini (2013), The UBO-TSUFD tsunami inundation model: Validation and application to a tsunami case study focused on the city of Catania, *Nat. Hazards Earth Syst. Sci.*, *13*, 1795–1816.
Titov, V. V., and F. I. González (1997), *Implementation and Testing of the Method of Splitting Tsunami (MOST) Model*, U. S. Dep. of Comm., Natl. Oceanic and Atmos. Admin., Environ. Res. Lab., Pac. Mar. Environ. Lab.
Toro, E. F. (2001), *Shock Capturing Methods for Free Surface Shallow Flows*, John Wiley, Chichester, U. K.
Toro, E. F. (2009), *Riemann Solvers and Numerical Methods for Fluid Dynamics*, 3rd revision, Springer, Berlin and Heidelberg.
Valiani, A., and L. Begnudelli (2006), Divergence form for bed slope source term in shallow water equations, *J. Hydraul. Eng.*, *327*, 652–665.
van Leer, B. (1974), Towards the ultimate conservative difference scheme II. Monotonicity and conservation combined in a second-order scheme, *J. Comput. Phys.*, *14*, 361–370.
Yeh, H., P. Liu, and C. Synolakis (1996), *Long-Wave Runup Models*, World Sci, U.S.A.
Zhou, L., D. M. Causon, C. G. Mingham, and D. M. Ingram (2002), Numerical solutions of the shallow water equations with discontinuous bed topography, *Int. J. Numer. Meth. Fluids*, *38*, 769–788.
Zhou, L., Q. Bao, Y. Liu, G. Wu, W.-C. Wang, X. Wang, B. He, H. Yu, and J. Li (2015), Global energy and water balance: Characteristics from finite-volume atmospheric model of the IAP/LASG, *J. Adv. Model. Earth Syst.*, *7*, 1–20, doi:10.1002/2014MS000349.